UC Berkeley

Title

A room temperature polar magnetic metal

Authors

Zhang, Hongrui
Shao, Yu-Tsun
Chen, Rui
et al.

Peer reviewed

A room temperature polar magnetic metal

Hongrui Zhang[1,10*], Yu-Tsun Shao[2,10], Rui Chen[1,3,10], Xiang Chen[3,4,10], Sandhya Susarla[1,3], David Raftrey[3,5], Jonathan T. Reichanadter[4,6], Lucas Caretta[1], Xiaoxi Huang[1], Nicholas S. Settineri[6], Zhen Chen[2], Jingcheng Zhou[1], Edith Bourret-Courchesne[3], Peter Ercius[7], Jie Yao[1,3], Peter Fischer[3, 5], Jeffrey B. Neaton[3,4,8], David A. Muller[2,9], Robert J. Birgeneau[3,4], Ramamoorthy Ramesh[1,3,4*]

[1] Department of Materials Science and Engineering, University of California, Berkeley, CA, USA.

[2] School of Applied and Engineering Physics, Cornell University, Ithaca, NY, USA.

[3] Materials Sciences Division, Lawrence Berkeley National Lab, Berkeley, CA, USA.

[4] Department of Physics, University of California, Berkeley, CA, USA.

[5] Physics Department, UC Santa Cruz, Santa Cruz, CA, USA

[6] Department of Electrical Engineering, University of California, Berkeley, CA, USA.

[7] The Molecular Foundry, Lawrence Berkeley National Laboratory, Berkeley, CA, USA.

[8] Kavli Energy Nanosciences Institute at Berkeley, Berkeley, CA, USA

[9] Kavli Institute at Cornell for Nanoscale Science, Cornell University, Ithaca, NY, USA.

[10] These authors contributed equally.

*Corresponding authors. Email: hongruizhang@berkeley.edu, rramesh@berkeley.edu

The emergence of long-range magnetic order in non-centrosymmetric compounds has stimulated interest in the possibility of exotic spin transport phenomena and topologically protected spin textures for applications in next generation spintronics. Polar magnets, with broken symmetries of spatial inversion and time reversal, usually host chiral spin textures. This work reports a novel wurtzite-structure polar magnetic metal, identified as AA'-stacked $(Fe_{0.5}Co_{0.5})_5GeTe_2$, which exhibits a Néel-type skyrmion lattice as well as a Rashba-Edelstein effect at room temperature. Atomic resolution imaging of the structure reveals a structural transition as a function of Co-substitution, leading to the emergence of the polar phase at 50% Co. This discovery reveals an unprecedented layered polar magnetic system for investigating intriguing spin topologies and ushers in a promising new framework for spintronics.

Non-centrosymmetric magnets offer an extraordinary platform for exploring fascinating magnetic, quantum topological phases, owing to broken crystal symmetries.[1-7] As an example, magnetic skyrmions[8-10] have been observed in polar magnets and are usually stabilized by an antisymmetric Dzyaloshinskii-Moriya interaction (DMI). In polar magnets such as GaV_4S_8 (C_{3v}) [11], $VOSe_2O_5$ (C_{4v})[12], GaV_4Se_8 (C_{3v})[13], and PtMnGa (C_{3v})[14] with C_{nv} crystal symmetry, the DMI confines the magnetic modulation direction vector to be perpendicular to the polar axis. Thus, a Néel-type skyrmion lattice is stable once a suitable magnetic field is applied along the polar axis. In addition, in polar metals or semiconductors[15,16], the crystal structure leads to a built-in electric potential along the polar axis and spin-orbit interaction, which is the essence of the Rashba effect[17]. The Rashba Hamiltonian can be expressed as: $H_R = a_R(\vec{k} \times \vec{\sigma}) \cdot \vec{z}$, where a_R is the Rashba coefficient, $\vec{k}$ is the momentum vector, $\vec{\sigma}$ is the Pauli matrix vector, and $\vec{z}$ is the unit vector along with the polar axis. In such a system, the Edelstein effect[18] is also observed, that is, a nonequilibrium spin accumulation occurs by applying an electric field to the spin-polarized bands. Thus, a highly efficient spin-to-charge conversion has been demonstrated in polar magnetic semiconductors[16] and interfacial systems[19-22]. Until now, no single phase, polar ferromagnetic metals have been observed at room temperature although multilayers comprised of ferromagnets (e.g., Co/Pt[8,23]) can show polar magnetic metal behavior.

In van der Waals (vdW) systems, the stacking configuration can be engineered to manipulate crystal symmetry, for example, by synthesis conditions[24], chemical doping[25] and external field[26], and thus plays a crucial role in mediating physical phenomena such as ferroelectricity, [27] magnetism,[28] and superconductivity[29]. Recent work reported that by capping a spin-orbit coupling layer on Fe_3GeTe_2 induces an interfacial DMI and skyrmions in this bilayer system below ambient temperature.[30-33] The Fe_5GeTe_2 system exhibits two-dimensional (2D) itinerant ferromagnetism with high Curie temperature which provides an ideal platform to design such a metallic, polar magnetic material. The vdW $Fe_{5-x}GeTe_2$ magnet exhibits rhombohedral ABC stacking with a ferromagnetic ground state.[34,35] Interestingly, the introduction of cobalt into the iron sites within this compound has been shown to induce a structural phase transition to the inversion-centric, hexagonal AA stacked $(Fe_{1-y},Co_y)_{5-x}GeTe_2$ (y = 0.44, 0.46) with an

antiferromagnetic ordering.[36,37] Here, we report the experimental discovery of a hexagonally-stacked $(Fe_{0.5}Co_{0.5})_5GeTe_2$ (FCGT) phase, denoted as AA'- stacked FCGT, by systematically increasing the cobalt doping to 50%. Distinct from the previously identified Fe_NGeTe_2 (N = 3, 4, 5) systems, the AA' stacked FCGT exhibits a polar crystal structure that shows ferromagnetic order with a remarkably high Curie temperature (T_c, ~350 K). As a result of this polar structure, we observe a well-ordered lattice of Néel-type skyrmions at room temperature probed directly via Lorentz scanning transmission electron microscopy (L-STEM), magnetic force microscopy (MFM) and magnetotransport measurements. Spin torque ferromagnetic resonance (ST-FMR) and second harmonic Hall measurement studies show a Rashba-Edelstein effect, illustrating the potential for use as both the ferromagnet and a spin-orbit torque metal in spintronic applications.

High-quality FCGT single crystals with the two different stacking symmetries were synthesized by tuning the cobalt concentration using a chemical vapor transport method (details of the synthesis are presented in the Methods section). The composition of the FCGT platelets was confirmed by energy dispersive X-ray spectroscopy (EDS), illustrated for the 45% Co and 50% Co platelets (see Supplemental Material Fig. S1 for details[38]). Armed with the chemical stoichiometry, then the atomic scale structure of these two platelets was studied. Pristine Fe_5GeTe_2 has an ABC stacking with a rhombohedral unit cell and space group $R\bar{3}m$ (No. 166); [36,37] introduction of cobalt of upto 40-47% atomic concentration transforms the FCGT crystal into the AA phase with the space group $P\bar{3}m1$ (No. 164).[36] Surprisingly, as the cobalt concentration is increased to 50%, the AA stacked FCGT transitions into the AA' stacking which belongs to the space group $P6_3mc$ (No. 186) (see Supplemental Material Methods and single-crystal X-ray diffraction data in Fig. S2 and Fig. S3 for details[38]). This space group with a polar point group indicates that the AA' stacking FCGT is a unique non-centrosymmetric structure in the Fe_NGeTe_2 system (N = 3,4,5). To understand the atomistic origins of inversion symmetry in the AA and AA' phases, scanning transmission electron microscopy (STEM) was performed. Fig. 1 illustrates the atomic configuration for the two types of FCGT, labelled as AA (Fig. 1**a**) and AA' stacking (Fig. 1**c**). High angle annular dark field-scanning transmission electron microscopy (HAADF-STEM) images of cross-sections in the [110] zone axis of the two platelets reveal strikingly different stacking information, shown in Fig. 1(**b, d**) and Fig. S4 and Fig.S5 (see Supplemental Material for details[38]). The corresponding simulated images are

shown to the right of the experimental images. The averaged intensity line traces for both these images reveal a significant difference, as shown in Fig.1(**g, h**). Both phases are built up of double Te layers between which the Fe/Co/Ge layers are stacked. The AA-phase (45% Co) has a predominance of 7-layer stacking with a minority of 6-layer stacking. In stark contrast, the AA' structure in the 50% Co sample has a predominance of 6-layer stacks with a minority of 5- and 7-layer stacks. It is also noteworthy that the three different Fe-sites (see Supplemental Material Fig. S3 for details[38]) are clearly not at the same intensity, hinting at the possibility of partial occupancy of these sites, particularly the Fe1a and Fe1b sites. This difference in stacking sequence between the two Te layers is captured at a larger scale in Fig.1(**e, f**) for the AA and the AA' phases, respectively. These images are false-color coded to illustrate the differences in stacking sequence, that was derived from atomic columns that were Gaussian-fitted to extract their exact positions. The bar charts to the right of Fig.1(**g, h**) summarize the statistics of the layer stacking for the AA and AA' phases. Thus, the Fe1a sites ordering in AA' phase FCGT breaks inversion symmetry, resulting in a net polar field along the c axis.
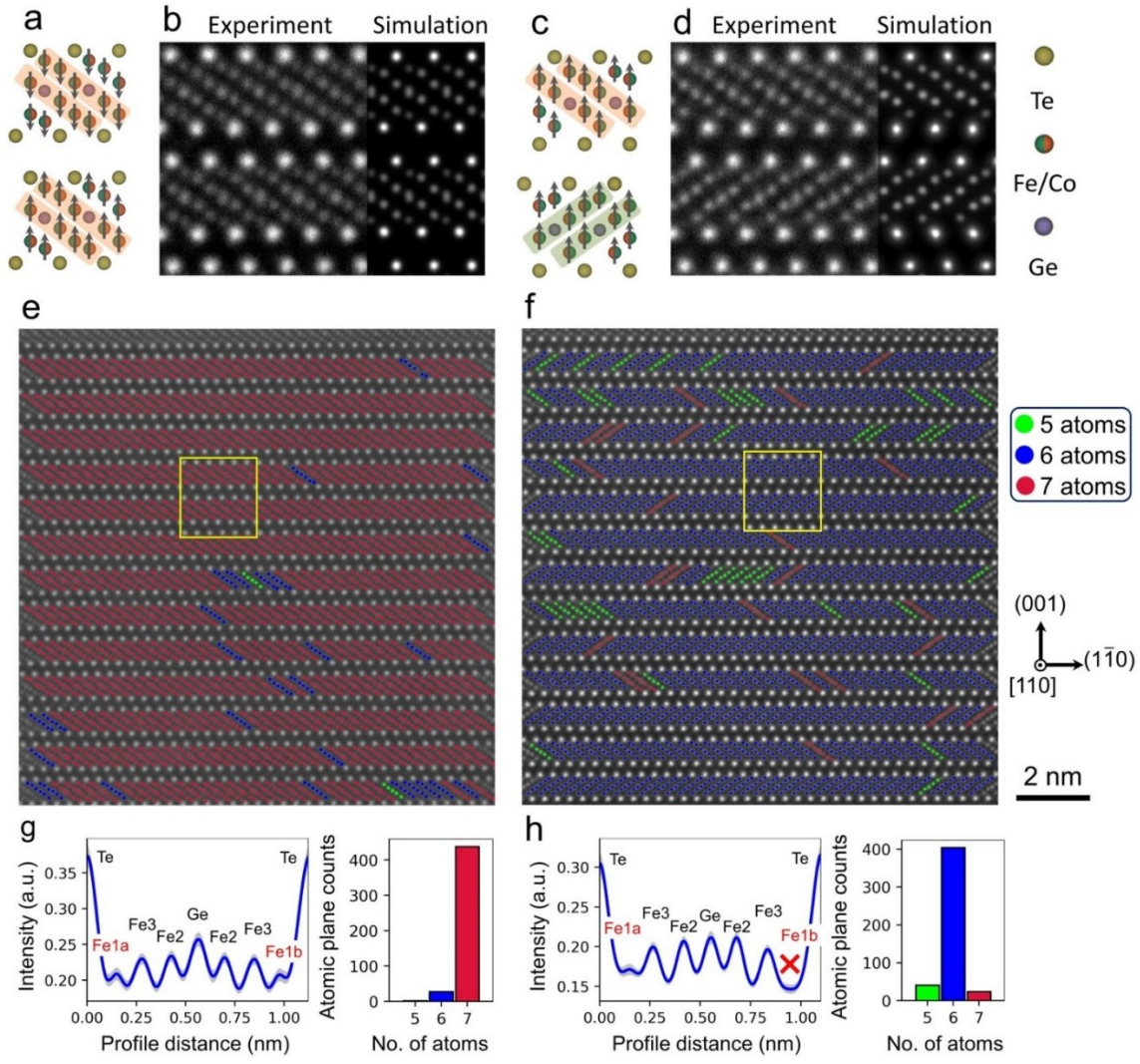
Fig. 1: Structural phase transition of $(Fe_{1-y}Co_y)_5GeTe_2$. a,b,c,d, Structure model and corresponding HAADF-STEM cross-sectional images of FCGT for (**a,b**) AA stacking (y=0.45) and (**c,d**) AA' stacking (y=0.50) along the [110] direction. The black arrows represent the corresponding evolution of magnetic order and anisotropy. Enlarged experimental and corresponding simulated HAADF-STEM images of a 10-nm-thick FCGT for AA-stacking (**b**) and (**d**) AA'-stacking phases. **e,f**, The Fe-Co-Ge-sub-lattices are color-coded by the number of atoms in the atomic planes, with 5(G), 6(B), 7(R) atoms, respectively. The yellow boxes in (**e, f**) indicate the regions for (**b, d**), respectively. **g,h**, Te-Te intensity line profiles and the histograms show the counts for the number of atoms in each sub-lattice plane. The gray shaded area indicates the standard deviation of the intensity profiles.

Armed with this atomic scale structural information, chemical mapping via simultaneous HAADF-STEM and electron energy loss spectroscopy (EELS) were performed. Details of the STEM-EELS acquisition parameters are described in the methods section. EELS maps for the individual chemical species (i.e., Te, Fe, Co, Ge) along with the ADF-STEM images are shown in Fig. S6 and Fig. S7 (see Supplemental Material for details[38]) and exemplar individual EELS spectra are shown in Fig. S8 (see Supplemental Material for details[38]). Fig. 2**a, b** shows the simultaneously acquired atomic resolution HAADF images for AA and AA' respectively, where we specifically focus on the Fe and Co EELS spectra. In order to distinguish between the atomic distribution of closely spaced (~1.3 Å apart) Fe (red) and Co (green) atoms, we calculated the intensity difference maps by subtracting the normalized Co intensity from the normalized Fe intensity as shown in the maps in Fig. 2**c,d**. The color scale used in the difference maps diverges from green to orange where green indicates enrichment of Co while orange indicates Fe enrichment. The zoomed-in HAADF and EELS maps that are displayed as insets in Fig. 2 show the location of these Co enrichment sites. In the AA phase, Co enrichment is mostly limited to the Fe-sites near the Ge atomic columns, i.e., Fe2 sites. However, in the AA' phase there are two Co sites that exhibit enrichment, namely Fe2 which is close to the Ge atoms, and Fe1 which is close to the Te atoms.
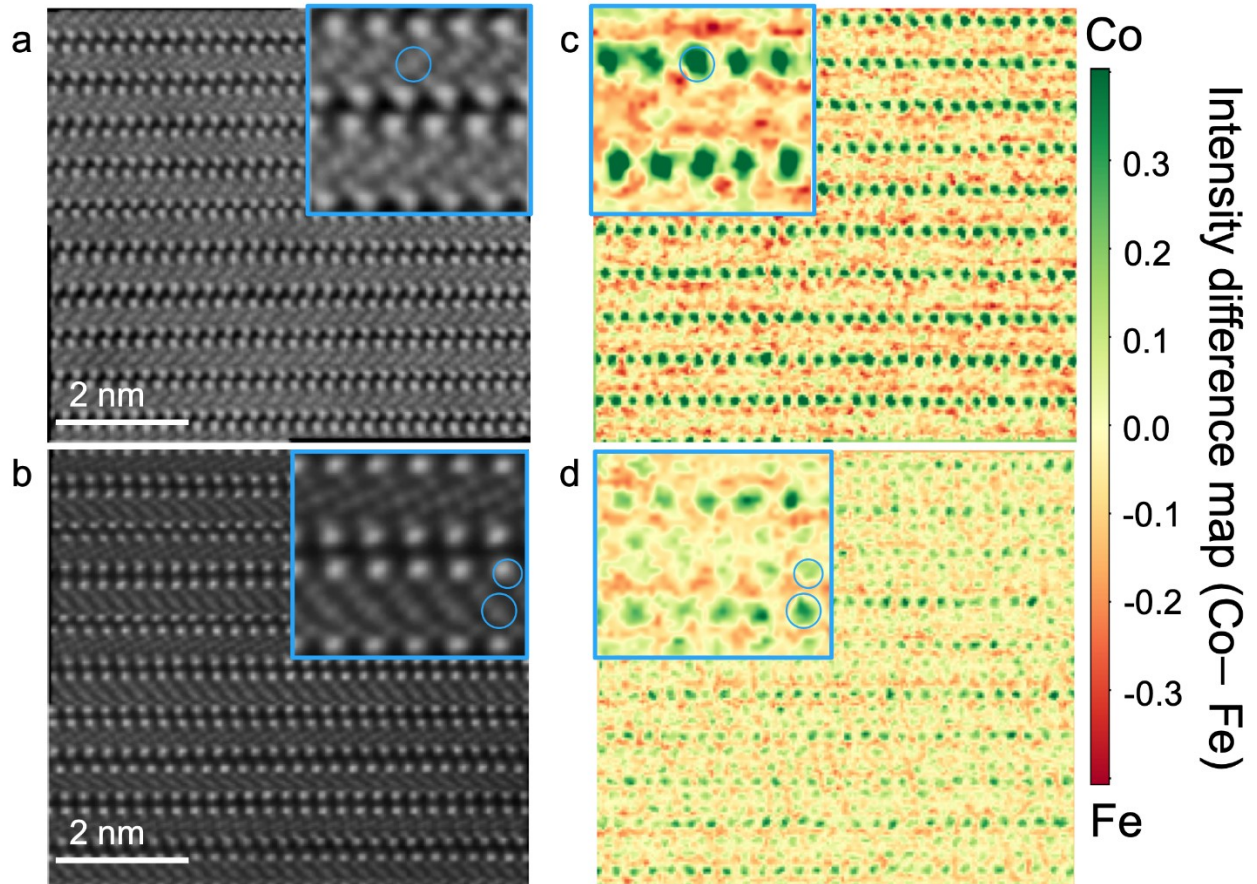
Fig. 2: Chemical distribution in CFGT. a, b, Simultaneous atomic resolution HAADF-STEM images for AA and AA' phase. **c, d,** Intensity difference EELS maps (Co - Fe) for AA and AA' phase. Inset indicates the zoomed-in images of the HAADF and EELS maps. Green coloring in the STEM-EELS maps indicates relatively higher cobalt concentration, and orange coloring indicates relatively higher iron concentration. The blue circles in the insets indicate the estimated delocalization radius of the EEL signal.

To provide insight into energetics of the centrosymmetric and polar phases of FCGT, density functional theory (DFT) calculations were performed using the exchange-correlation functional of Perdew, Burke, and Ernzerhof (PBE)[39] and Hubbard U[40] and Grimme D3 van der Waals corrections[39] for the pristine stoichiometric endpoint compounds Fe_5GeTe_2 and Co_5GeTe_2, assuming collinear magnetic order and a fixed Fe1a site occupancy (see Methods for details). The atomic positions and lattice parameters of Fe_5GeTe_2 and Co_5GeTe_2 for the ABC, AA, and AA' phases with fixed Fe1a site occupancies were optimized with DFT-PBE+U+D3 for both

ferromagnetic and antiferromagnetic inter-planar order. The ground-state energy per formula unit (f.u.) was computed from each relaxed geometry and appears in Table S1, along with details of each configuration's lattice parameters and magnetic order.

The DFT ground-state energies for ABC, AA, and AA' structural and magnetic phases considered lie within about ±10 meV/f.u., strongly supporting the hypothesis that each relevant polytype is experimentally accessible. From the relaxed lattice parameters in Table S1, we identify a significant reduction of the out-of-plane c lattice parameter (1.7% for Fe_5GeTe_2 and 1.3% for Co_5GeTe_2) in the polar AA' phase relative to the nonpolar AA and ABC structural phases for both Fe and Co compounds species. This is consistent with the XRD measurements of the AA' FCGT crystal (see Supplemental Material Fig. S2 and Fig. S3 for details[38]), which show a reduction in the c lattice parameter from AA to AA' phases of similar composition. The computed intralayer spacings-i.e., the interplanar spacings of adjacent Fe/Co/Ge layers- for all relaxed structures and magnetic orders considered were calculated to be very similar for the different structural phases, with the c lattice parameter reduction largely resulting from a change in interlayer spacing-i.e., the vdW spacing between adjacent Te layers- unique to the AA' phase. This reduction may also suggest that the distinct magnetic ordering behavior of this novel AA' phase is influenced by a distance-sensitive interlayer exchange.

Temperature-dependent transport measurements of an AA' phase FCGT nanoflake exhibit a typical metallic behavior (Fig. 3**a**; inset shows the Hall bar device), and the corresponding magnetic field dependence of the Hall resistance (R_{xy}) at various temperatures is shown in Fig. 3**b**. At 10 K, R_{xy} shows a rectangular hysteresis loop as a function of out-of-plane magnetic field, indicating a ferromagnetic ground state and a fully-remnant, single magnetic domain state. At ~ 70 K, the Hall data shows a sheared out-of-plane hysteresis loop suggesting the onset of labyrinthine domains.[41] At higher temperatures (70-320 K), the sheared hysteresis loop remains while the saturation field gradually decreases. Finally, for temperatures higher than 325 K, the sheared hysteresis loops disappear. The value of R_{AHE} is ~ 0.25 Ω at 10 K, and the saturated R_{AHE} in Fig. 3**b** decreases with increasing temperature, revealing a surprisingly high T_c of ~ 350 K (Fig. 3**c**), which is consistent with the bulk magnetization measurements. The magnetotransport data along with the structural information in Fig.1 establish AA'-stacked FCGT as a polar, magnetic metal.
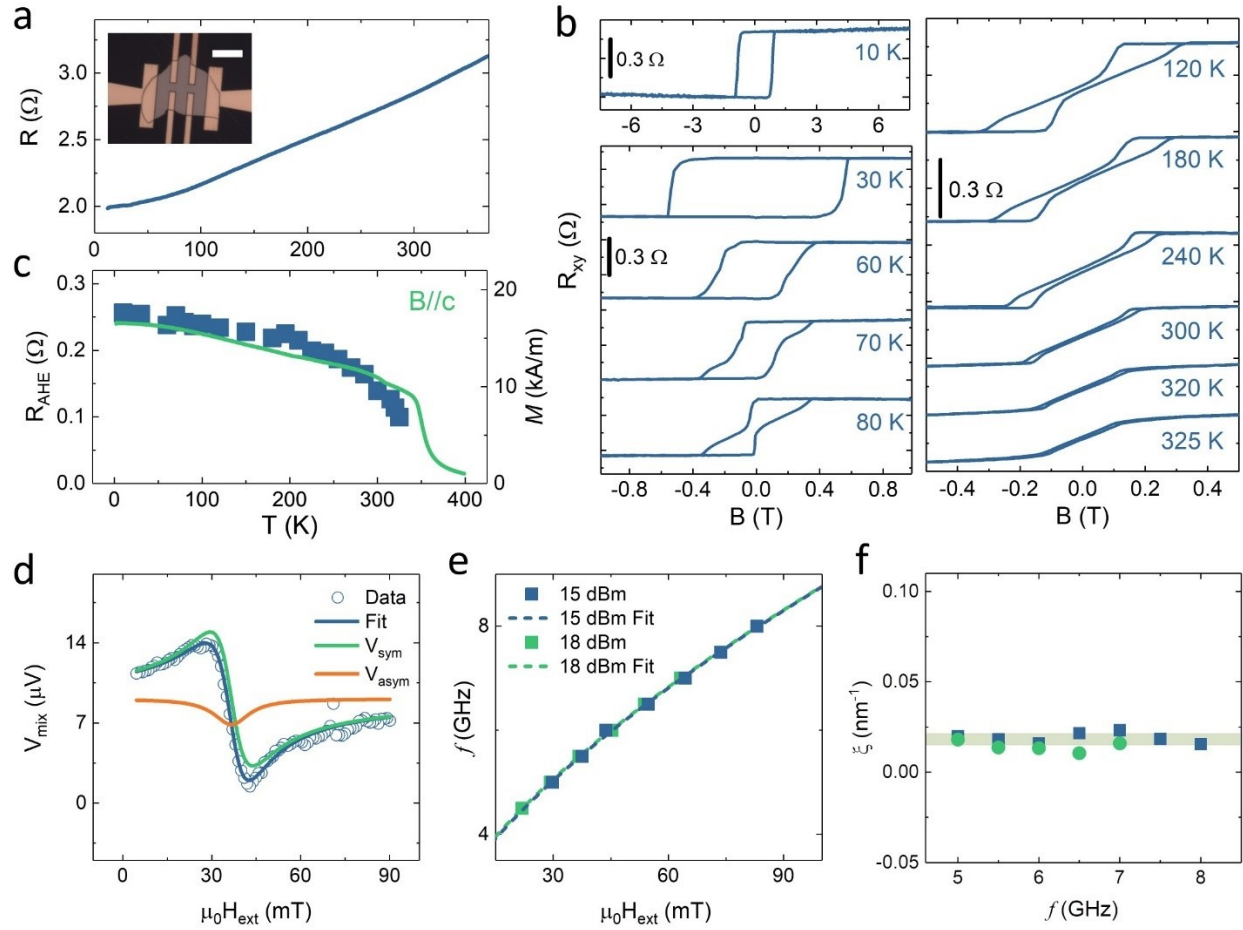
Fig. 3: Magnetotransport and ST-FMR measurements of an AA' phase FCGT nanoflakes.
a, Temperature dependence of the longitudinal resistance. The Hall bar device shown in the inset of (a) is based on a 200-nm-thick FCGT nanoflake on a SiO_2/Si substrate. The scale bar is 10 μm. **b**, Hall resistance versus magnetic field at select temperatures. **c**, Temperature dependence of the anomalous Hall resistance (blue square) in the saturation region. Temperature dependence of the magnetization (green line) was obtained at 5 mT. **d,** The ST-FMR signal of an FCGT (21 nm, ~11unit cells)/$Co_{0.9}Fe_{0.1}$(12 nm) sample at 5.5 GHz, 18 dBm. The solid lines are fits that show the symmetric (orange) and antisymmetric (yellow) Lorentzian contribution. **e,** ST-FMR frequency as a function of resonance field; the blue (15dBm) and green (18dBm) line is a fit to the Kittel formula. **f,** Charge to spin conversion coefficient (ξ) (details in the Methods section) as a function of frequency at 15 dBm and 18 dBm.

Based on the experimental demonstrations of the unique structure and magnetic characteristic for AA' phase FCGT, in the following, the novel electrical and magnetic properties are presented. In wurtzite structure materials, due to the broken inversion symmetry, spin-orbit interaction causes splitting of the electronic band structure, leading to the Rashba effect. To verify such current induced spin-orbit torques (SOTs) in the AA' phase, we performed Spin Torque Ferromagnetic Resonance (ST-FMR) measurements on multiple samples at room temperature. A typical ST-FMR signal for an AA'-FCGT/$Co_{0.9}Fe_{0.1}$ sample is shown in Fig. 3**d**; Fig. S12 (see Supplemental Material for details[38]) shows details of the measurement. This spectrum can be fitted well to a sum of symmetric (V_{sym}) and asymmetric components (V_{asym}) (see Methods section), which are proportional to the in-plane damping-like torque and out-of-plane torques, respectively. Fig. 3**e** shows the ST-FMR frequency as a function of resonant field, which is in good agreement with the Kittel formula[42,43], leading to an effective magnetization of the AA'-FCGT/$Co_{0.9}Fe_{0.1}$ bilayer of 626 kA/m. The charge-to-spin conversion coefficient (ξ) as the function of frequency is essentially constant, as shown in Fig. 3**f.** The average ξ of AA'-FCGT/$Co_{0.9}Fe_{0.1}$ system is ~ 0.017±0.003 nm^{-1}. In addition, an ST-FMR signal for an AA-FCGT/CoFe sample was also observed (see Supplemental Material Fig. S13 for details[38]) The average ξ of AA-FCGT/$Co_{0.9}Fe_{0.1}$ is close to that of the AA'-FCGT/CoFe system. Due to the AA-FCGT without breaking inversion symmetry, this implies that the ST-FMR signal of AA'-FCGT/$Co_{0.9}Fe_{0.1}$ sample may be original from the Rashba-Edelstein effect of the Te/$Co_{0.9}Fe_{0.1}$ interface or the spin Hall effect from the FCGT system. In order to verify the existence of the bulk Rashba-Edelstein effect in this system, the second harmonic Hall measurements were performed in the 100-nm-thick AA' phase of a single layer FCGT nanoflake (see Supplemental Material Fig. S14 for details[38]). The behavior we observed is similar to the result of the bulk magnetic Rashba system, Mn-doped GeTe.[16] By analysis, it gives a charge-to-spin conversion coefficient of $\xi \sim 0.024$ nm^{-1}. Even the second harmonic signal was observed in the single-layer AA' FCGT, more approaches are still needed to distinguish the three contributions of the ST-FMR signal in detail in future work.

A polar magnet, which exhibits a sheared hysteresis loop, might be expected to formation of Néel-type skyrmion(s) in finite external magnetic fields. To verify this, Lorentz TEM (LTEM) measurements was performed on the AA' phase FCGT nanoflakes at room temperature to image

the multidomain ground state. LTEM imaging was performed on a 110 nm-thick FCGT flake at a defocus of +4 mm at room temperature (Figs. 4**a**-4**c**). At zero applied magnetic field, no magnetic contrast was observed at normal incidence (Fig. 4**a**); labyrinthine domains are visible (Fig. 4**b**) once the sample is tilted by 18° around the horizontal imaging direction as indicated in Fig. 4**a**. At zero tilt, the electron deflection cancels out due to the symmetric distribution of magnetization and thus the images exhibit no contrast in the standard LTEM mode.[44,45] An external field applied in the LTEM along the beam direction triggers a domain morphology evolution from stripes to a mixture of bubbles and much shorter stripes (see Supplemental Material Fig. S15 for details[38])). When the magnetic field is increased up to 139 mT, we find that the bubbles clearly show dark/bright contrast perpendicular to the tilt axis, indicating Néel-type skyrmions (Fig. 4**c**). Finally, when the magnetic field is increased to 160 mT, the sample is magnetically saturated into a single domain state.
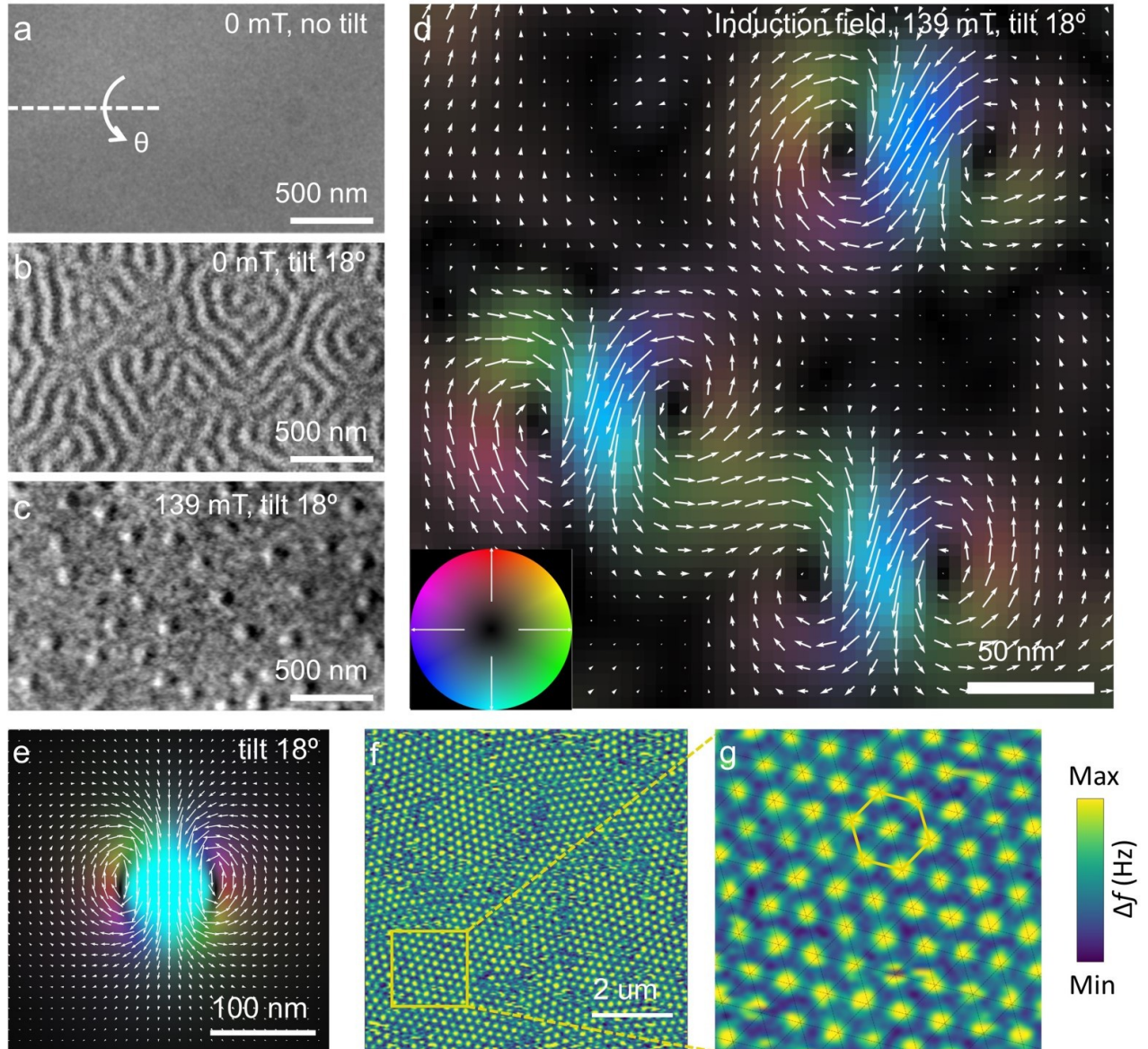
Fig. 4: Room temperature spin texture of AA' phase FCGT. a, b, Lorentz TEM images of the 110 nm-thick nanoflake acquired at the same region under zero-field and +4 mm defocus with 0°-tilt and 18°-tilt reveal a labyrinth phase with Neél character. **c,** In the same region at an 18°-tilt angle, isolated skyrmions emerge with an applied field of 139 mT. The skyrmion size is ~90 nm, determined from the lateral distance between the minimum and maximum intensity profile of the bubbles. **d,** Magnetic induction map obtained using four-dimensional Lorentz STEM (4D-LSTEM) equipped with an electron microscopy pixel array detector (EMPAD). The color and arrows indicate induction field components of Néel skyrmions perpendicular to the beam propagation direction for an 18° sample tilt. **e,** Simulated magnetic induction map for a Neél

skyrmion at an 18°-tilt. **f,** MFM images of an FCGT nanoflake on a SiO_2/Si substrate. The thickness is ~ 128 nm, obtained by line profile of atomic force microscopy. **g,** High magnification of the skyrmion lattice region indicated by the yellow box in **f**. The skyrmion lattice parameter is ~ 200 nm corresponding to a density of ~23.3 skyrmions/μm^2.

To elucidate the detailed structure of such Néel-type skyrmions, four-dimensional LSTEM (4D-LSTEM) experiments were performed using a high-dynamic-range electron microscopy pixel array detector (EMPAD).[46] 4D-LSTEM works by acquiring a full 2D, angle-resolved scattering distribution at each probe scanning position in a 2D grid, resulting in four-dimensional datasets. By quantitatively measuring the scattering distribution at each point in real space, 4D-LSTEM can detect the phase shift of the electron beam induced by the lateral magnetic induction field of the spin textures (Fig. 4d). The magnetic induction field of Néel-type skyrmions (Fig. 4**d**) can thus be derived from the deflection of the electron beam in each diffraction pattern due to the Lorentz force, where the color and arrows represent the direction of the projected in-plane components.[47] A magnetic induction composed of clockwise and counter-clockwise spin curls was observed, which agrees well with the calculated induction field distribution for Néel- type magnetic skyrmions, Fig. 4**e** and Fig. S16 (see Supplemental Material for details[38]).[45,48] The formation of skyrmions is also verified by magnetic force microscopy imaging illustrated in Fig.4(**f,g**). We observe an ordered hexagonal skyrmion lattice at room temperature and zero field with a lattice parameter of ~200 nm corresponding to a density of ~ 23.3 skyrmions/μm^2. The zero-field skyrmion lattice is induced by the stray field of the MFM tips.

Based on these experimental demonstrations of skyrmions in the AA' phase FCGT system, the physical origins of DMI are now discussed. The AA' phase FCGT is a polar magnet with a C_{6v} point group. The direction of effective DMI is perpendicular to the polar axis (*c*-axis), i.e., in-plane. Therefore, we carried out micromagnetic simulations to estimate the DMI constant at room temperature (see Supplemental Material Method and Fig. S17 for details[38]). We simulated a 1μm × 1μm sample with a thickness of 110 nm, which is the same thickness as the sample imaged with LTEM. Given the simulation results, we found that as the DMI value increases, the domain pattern transitions from isolated skyrmions to a skyrmion lattice while its

size decreases. By comparing the LTEM experimental results with the simulations, we estimated a value of the effective DMI constant of ~ 0.95 mJ/m^2.

The observation of a polar ferromagnetic metal at room temperature opens up exciting fundamental opportunities, with the potential to impact applications in spintronics. Our work clearly demonstrates the role of structural and chemical order, along with the subtle changes in electronic and spin structure through Co substitution, in triggering the broken inversion symmetry of the underlying crystal. This directly leads to the emergence of a bulk Dzyalozhinski-Moriya coupling and Rashba-type spin-orbit coupling which are fundamental requirements for both the formation of Néel -type skyrmions as well as the occurrence of a Rashba-Edelstein effect. This work shows enormous potential for crystal symmetry control of the spin and electric quantum state of the materials.

Acknowledgements:

Reference:

[1]   X. Z. Yu, Y. Onose, N. Kanazawa, J. H. Park, J. H. Han, Y. Matsui, N. Nagaosa, and Y. Tokura, Real-space observation of a two-dimensional skyrmion crystal Nature **465**, 901 (2010).

[2]   K. Karube, J. S. White, N. Reynolds, J. L. Gavilano, H. Oike, A. Kikkawa, F. Kagawa, Y. Tokunaga, H. M. Ronnow, Y. Tokura, and Y. Taguchi, Robust metastable skyrmions and their triangular-square lattice structural transition in a high-temperature chiral magnet Nature Mater. **15**, 1237 (2016).

[3]   C. Ciccarelli, L. Anderson, V. Tshitoyan, A. J. Ferguson, F. Gerhard, C. Gould, L. W. Molenkamp, J. Gayles, J. Železný, L. Šmejkal, Z. Yuan, J. Sinova, F. Freimuth, and T. Jungwirth, Room-temperature spin–orbit torque in NiMnSb Nature Phys. **12**, 855 (2016).

[4]   S. Mühlbauer, B. Binz, F. Jonietz, C. Pfleiderer, A. Rosch, A. Neubauer, G. R., and P. Böni, Skyrmion Lattice in a Chiral Magnet Science **323**, 915 (2009).

[5]   P. Wadley, B. Howells, J. Železný, C. Andrews, V. Hills, R. P. Campion, V. Novák, K. Olejník, F. Maccherozzi, S. S. Dhesi, S. Y. Martin, T. Wagner, J. Wunderlich, F. Freimuth, Y. Mokrousov, J. Kuneš, J. S. Chauhan, M. J. Grzybowski, A. W. Rushforth, K. W. Edmonds, B. L. Gallagher, and T. Jungwirth, Electrical switching of an antiferromagnet Science **351**, 587 (2016).

[6]   X. Chen, S. Shi, G. Shi, X. Fan, C. Song, X. Zhou, H. Bai, L. Liao, Y. Zhou, H. Zhang, A. Li, Y. Chen, X. Han, S. Jiang, Z. Zhu, H. Wu, X. Wang, D. Xue, H. Yang, and F. Pan, Observation of the antiferromagnetic spin Hall effect Nature Mater. **20**, 800 (2021).

[7]   R. Chen, F. Luo, Y. Liu, Y. Song, Y. Dong, S. Wu, J. Cao, F. Yang, A. N'Diaye, P. Shafer, Y. Liu, S. Lou, J. Huang, X. Chen, Z. Fang, Q. Wang, D. Jin, R. Cheng, H. Yuan, R. J. Birgeneau, and J. Yao, Tunable room-temperature ferromagnetism in Co-doped two-dimensional van der Waals ZnO Nat. Commun. **12**, 3952 (2021).

[8]   S. Woo, K. Litzius, B. Kruger, M. Y. Im, L. Caretta, K. Richter, M. Mann, A. Krone, R. M. Reeve, M. Weigand, P. Agrawal, I. Lemesh, M. A. Mawass, P. Fischer, M. Klaui, and G. S. Beach, Observation of room-temperature magnetic skyrmions and their current-driven dynamics in ultrathin metallic ferromagnets Nature Mater. **15**, 501 (2016).

[9]   A. Fert, N. Reyren, and V. Cros, Magnetic skyrmions: advances in physics and potential applications Nat. Rev. Mater. **2**, 17031 (2017).

[10]   O. Boulle, J. Vogel, H. Yang, S. Pizzini, D. de Souza Chaves, A. Locatelli, T. O. Mentes, A. Sala, L. D. Buda-Prejbeanu, O. Klein, M. Belmeguenai, Y. Roussigne, A. Stashkevich, S. M. Cherif, L. Aballe, M. Foerster, M. Chshiev, S. Auffret, I. M. Miron, and G. Gaudin, Room-temperature chiral magnetic skyrmions in ultrathin magnetic nanostructures Nature Nanotech. **11**, 449 (2016).

[11]   I. Kezsmarki, S. Bordacs, P. Milde, E. Neuber, L. M. Eng, J. S. White, H. M. Ronnow, C. D. Dewhurst, M. Mochizuki, K. Yanai, H. Nakamura, D. Ehlers, V. Tsurkan, and A. Loidl, Neel-type skyrmion lattice with confined orientation in the polar magnetic semiconductor GaV_4S_8 Nature Mater. **14**, 1116 (2015).

[12]   T. Kurumaji, T. Nakajima, V. Ukleev, A. Feoktystov, T. H. Arima, K. Kakurai, and Y. Tokura, Neel-Type Skyrmion Lattice in the Tetragonal Polar Magnet $VOSe_2O_5$ Phys. Rev. Lett. **119**, 237201 (2017).

[13]   Y. Fujima, N. Abe, Y. Tokunaga, and T. Arima, Thermodynamically stable skyrmion lattice at low temperatures in a bulk crystal of lacunar spinel GaV_4Se_8 Phys. Rev. B **95**, 180410(R) (2017).

[14]   A. K. Srivastava, P. Devi, A. K. Sharma, T. Ma, H. Deniz, H. L. Meyerheim, C. Felser, and S. S. P. Parkin, Observation of Robust Neel Skyrmions in Metallic PtMnGa Adv. Mater. **32**, 1904327 (2020).

[15]   K. Ishizaka, M. S. Bahramy, H. Murakawa, M. Sakano, T. Shimojima, T. Sonobe, K. Koizumi, S. Shin, H. Miyahara, A. Kimura, K. Miyamoto, T. Okuda, H. Namatame, M. Taniguchi, R. Arita,

N. Nagaosa, K. Kobayashi, Y. Murakami, R. Kumai, Y. Kaneko, Y. Onose, and Y. Tokura, Giant Rashba-type spin splitting in bulk BiTeI Nature Mater. **10**, 521 (2011).

[16] R. Yoshimi, K. Yasuda, A. Tsukazaki, K. S. Takahashi, M. Kawasaki, and Y. Tokura, Current-driven magnetization switching in ferromagnetic bulk Rashba semiconductor (Ge,Mn)Te Sci. Adv. **4**, eaat9989 (2018).

[17] A. Manchon, H. C. Koo, J. Nitta, S. M. Frolov, and R. A. Duine, New perspectives for Rashba spin–orbit coupling Nature Mater. **14**, 871 (2015).

[18] V. M. Edelstein, Spin polarization of conduction electrons induced by electric current in two-dimensional asymmetric electron systems Solid State Commun. **73**, 233 (1990).

[19] I. Mihai Miron, G. Gaudin, S. Auffret, B. Rodmacq, A. Schuhl, S. Pizzini, J. Vogel, and P. Gambardella, Current-driven spin torque induced by the Rashba effect in a ferromagnetic metal layer Nature Mater. **9**, 230 (2010).

[20] E. Lesne, Y. Fu, S. Oyarzun, J. C. Rojas-Sánchez, D. C. Vaz, H. Naganuma, G. Sicoli, J. P. Attané, M. Jamet, E. Jacquet, J. M. George, A. Barthélémy, H. Jaffrès, A. Fert, M. Bibes, and L. Vila, Highly efficient and tunable spin-to-charge conversion through Rashba coupling at oxide interfaces Nature Mater. **15**, 1261 (2016).

[21] Q. Song, H. Zhang, T. Su, W. Yuan, Y. Chen, W. Xing, J. Shi, J. Sun, and W. Han, Observation of inverse Edelstein effect in Rashba-split 2DEG between $SrTiO_3$ and $LaAlO_3$ at room temperature Sci. Adv. **3**, e1602312 (2017).

[22] H. Zhang, Y. Ma, H. Zhang, X. Chen, S. Wang, G. Li, Y. Yun, X. Yan, Y. Chen, F. Hu, J. Cai, B. Shen, W. Han, and J. Sun, Thermal Spin Injection and Inverse Edelstein Effect of the Two-Dimensional Electron Gas at $EuO–KTaO_3$ Interfaces Nano Lett. **19**, 1605 (2019).

[23] C. O. Avci, K. Garello, A. Ghosh, M. Gabureac, S. F. Alvarado, and P. Gambardella, Unidirectional spin Hall magnetoresistance in ferromagnet/normal metal bilayers Nature Phys. **11**, 570 (2015).

[24] L. M. Schneider, J. Kuhnert, S. Schmitt, W. Heimbrodt, U. Huttner, L. Meckbach, T. Stroucken, S. W. Koch, S. Fu, X. Wang, K. Kang, E.-H. Yang, and A. Rahimi-Iman, Spin-Layer and Spin-Valley Locking in CVD-Grown AA′-and AB-Stacked Tungsten-Disulfide Bilayers J. Phys. Chem. C **123**, 21813 (2019).

[25] D. Rhodes, D. A. Chenet, B. E. Janicek, C. Nyby, Y. Lin, W. Jin, D. Edelberg, E. Mannebach, N. Finney, A. Antony, T. Schiros, T. Klarr, A. Mazzoni, M. Chin, Y. C. Chiu, W. Zheng, Q. R. Zhang, F. Ernst, J. I. Dadap, X. Tong, J. Ma, R. Lou, S. Wang, T. Qian, H. Ding, R. M. Osgood, Jr., D. W. Paley, A. M. Lindenberg, P. Y. Huang, A. N. Pasupathy, M. Dubey, J. Hone, and L. Balicas, Engineering the Structural and Electronic Phases of $MoTe_2$ through W Substitution Nano Lett. **17**, 1616 (2017).

[26] S. Cho, S. Kim, J. H. Kim, J. Zhao, J. Seok, D. H. Keum, J. Baik, D.-H. Choe, K. J. Chang, K. Suenaga, S. W. Kim, Y. H. Lee, and H. Yang, Phase patterning for ohmic homojunction contact in $MoTe_2$ Science **349**, 625 (2015).

[27] Z. Fei, W. Zhao, T. A. Palomaki, B. Sun, M. K. Miller, Z. Zhao, J. Yan, X. Xu, and D. H. Cobden, Ferroelectric switching of a two-dimensional metal Nature **560**, 336 (2018).

[28] B. Huang, G. Clark, E. Navarro-Moratalla, D. R. Klein, R. Cheng, K. L. Seyler, D. Zhong, E. Schmidgall, M. A. McGuire, D. H. Cobden, W. Yao, D. Xiao, P. Jarillo-Herrero, and X. Xu, Layer-dependent ferromagnetism in a van der Waals crystal down to the monolayer limit Nature **546**, 270 (2017).

[29] E. Morosan, H. W. Zandbergen, B. S. Dennis, J. W. G. Bos, Y. Onose, T. Klimczuk, A. P. Ramirez, N. P. Ong, and R. J. Cava, Superconductivity in Cu_xTiSe_2 Nature Phys. **2**, 544 (2006).

[30] Y. Wu, S. Zhang, J. Zhang, W. Wang, Y. L. Zhu, J. Hu, G. Yin, K. Wong, C. Fang, C. Wan, X. Han, Q. Shao, T. Taniguchi, K. Watanabe, J. Zang, Z. Mao, X. Zhang, and K. L. Wang, Néel-type skyrmion in WTe_2/Fe_3GeTe_2 van der Waals heterostructure Nat. Commun. **11**, 3860 (2020).

[31] B. Ding, Z. Li, G. Xu, H. Li, Z. Hou, E. Liu, X. Xi, F. Xu, Y. Yao, and W. Wang, Observation of Magnetic Skyrmion Bubbles in a van der Waals Ferromagnet Fe_3GeTe_2 Nano Lett. **20**, 868 (2020).

[32] M. Yang, Q. Li, R. V. Chopdekar, R. Dhall, J. Turner, J. D. Carlström, C. Ophus, C. Klewe, P. Shafer, A. T. N'Diaye, J. W. Choi, G. Chen, Y. Z. Wu, C. Hwang, F. Wang, and Z. Q. Qiu, Creation of skyrmions in van der Waals ferromagnet Fe_3GeTe_2 on $(Co/Pd)_n$ superlattice Sci. Adv. **6**, eabb5157 (2020).

[33] T. Xu, Z. Chen, H.-A. Zhou, Z. Wang, Y. Dong, L. Aballe, M. Foerster, P. Gargiani, M. Valvidares, D. M. Bracher, T. Savchenko, A. Kleibert, R. Tomasello, G. Finocchio, S.-G. Je, M.-Y. Im, D. A. Muller, and W. Jiang, Imaging the spin chirality of ferrimagnetic Néel skyrmions stabilized on topological antiferromagnetic Mn_3Sn Phys. Rev. Mater. **5**, 084406 (2021).

[34] H. Zhang, R. Chen, K. Zhai, X. Chen, L. Caretta, X. Huang, R. V. Chopdekar, J. Cao, J. Sun, J. Yao, R. Birgeneau, and R. Ramesh, Itinerant ferromagnetism in van der Waals $Fe_{5-x}GeTe_2$ crystals above room temperature Phys. Rev. B **102**, 064417 (2020).

[35] A. F. May, D. Ovchinnikov, Q. Zheng, R. Hermann, S. Calder, B. Huang, Z. Fei, Y. Liu, X. Xu, and M. A. McGuire, Ferromagnetism Near Room Temperature in the Cleavable van der Waals Crystal Fe_5GeTe_2 ACS nano **13**, 4436 (2019).

[36] A. F. May, M.-H. Du, V. R. Cooper, and M. A. McGuire, Tuning magnetic order in the van der Waals metal Fe_5GeTe_2 by cobalt substitution Phys. Rev. Mater. **4**, 074008 (2020).

[37] C. Tian, F. Pan, S. Xu, K. Ai, T. Xia, and P. Cheng, Tunable magnetic properties in van der Waals crystals $(Fe_{1-x}Co_x)_5GeTe_2$ Appl. Phys. Lett. **116**, 202402 (2020).

[38] See Supplemental Material at... for methods and additional analysis of structural and magnetic properties in the AA and AA' phase FCGT system.

[39] J. P. Perdew, K. Burke, and M. Ernzerhof, Generalized Gradient Approximation Made Simple Phys. Rev. Lett. **77**, 3865 (1996).

[40] S. L. Dudarev, G. A. Botton, S. Y. Savrasov, C. J. Humphreys, and A. P. Sutton, Electron-energy-loss spectra and the structural stability of nickel oxide: An LSDA+U study Phys. Rev. B **57**, 1505 (1998).

[41] Z. Fei, B. Huang, P. Malinowski, W. Wang, T. Song, J. Sanchez, W. Yao, D. Xiao, X. Zhu, A. F. May, W. Wu, D. H. Cobden, J. H. Chu, and X. Xu, Two-dimensional itinerant ferromagnetism in atomically thin Fe_3GeTe_2 Nature Mater. **17**, 778 (2018).

[42] L. Liu, T. Moriyama, D. C. Ralph, and R. A. Buhrman, Spin-Torque Ferromagnetic Resonance Induced by the Spin Hall Effect Phys. Rev. Lett. **106**, 036601 (2011).

[43] X. Huang, S. Sayed, J. Mittelstaedt, S. Susarla, S. Karimeddiny, L. Caretta, H. Zhang, V. A. Stoica, T. Gosavi, F. Mahfouzi, Q. Sun, P. Ercius, N. Kioussis, S. Salahuddin, D. C. Ralph, and R. Ramesh, Novel Spin–Orbit Torque Generation at Room Temperature in an All-Oxide Epitaxial $La_{0.7}Sr_{0.3}MnO_3/SrIrO_3$ System Adv. Mater. **33**, 2008269 (2021).

[44] M. J. Benitez, A. Hrabec, A. P. Mihai, T. A. Moore, G. Burnell, D. McGrouther, C. H. Marrows, and S. McVitie, Magnetic microscopy and topological stability of homochiral Neel domain walls in a $Pt/Co/AlO_x$ trilayer Nat. Commun. **6**, 8957 (2015).

[45] S. D. Pollard, J. A. Garlow, J. Yu, Z. Wang, Y. Zhu, and H. Yang, Observation of stable Neel skyrmions in cobalt/palladium multilayers with Lorentz transmission electron microscopy Nat. Commun. **8**, 14761 (2017).

[46] M. W. Tate, P. Purohit, D. Chamberlain, K. X. Nguyen, R. Hovden, C. S. Chang, P. Deb, E. Turgut, J. T. Heron, D. G. Schlom, D. C. Ralph, G. D. Fuchs, K. S. Shanks, H. T. Philipp, D. A. Muller, and S. M. Gruner, High Dynamic Range Pixel Array Detector for Scanning Transmission Electron Microscopy Microsc. Microanal. **22**, 237 (2016).

[47] M. Krajnak, D. McGrouther, D. Maneuski, V. O. Shea, and S. McVitie, Pixelated detectors and improved efficiency for magnetic imaging in STEM differential phase contrast Ultramicroscopy **165**, 42 (2016).

Supplementary Materials of "A room temperature polar ferromagnetic metal"

Hongrui Zhang[1,10*], Yu-Tsun Shao[2,10], Rui Chen[1,3,10], Xiang Chen[3,4,10], Sandhya Susarla[1,3], David Raftrey[3,5], Jonathan T. Reichanadter[4,6], Lucas Caretta[1], Xiaoxi Huang[1], Nicholas S. Settineri[6], Zhen Chen[2], Jingcheng Zhou[1], Edith Bourret-Courchesne[3], Peter Ercius[7], Jie Yao[1,3], Peter Fischer[3, 5], Jeffrey B. Neaton[3,4,8], David A. Muller[2,9], Robert J. Birgeneau[3,4], Ramamoorthy Ramesh[1,3,4*]

[1] Department of Materials Science and Engineering, University of California, Berkeley, CA, USA.

[2] School of Applied and Engineering Physics, Cornell University, Ithaca, NY, USA.

[3] Materials Sciences Division, Lawrence Berkeley National Lab, Berkeley, CA, USA.

[4] Department of Physics, University of California, Berkeley, CA, USA.

[5] Physics Department, UC Santa Cruz, Santa Cruz, CA, USA

[6] Department of Electrical Engineering, University of California, Berkeley, CA, USA.

[7] The Molecular Foundry, Lawrence Berkeley National Laboratory, Berkeley, CA, USA.

[8] Kavli Energy Nanosciences Institute at Berkeley, Berkeley, CA, USA

[9] Kavli Institute at Cornell for Nanoscale Science, Cornell University, Ithaca, NY, USA.

[10] These authors contributed equally.

*Corresponding authors. Email: hongruizhang@berkeley.edu, rramesh@berkeley.edu

Methods

Sample synthesis

Single crystals of $(Fe_{1-y}Co_y)_{5-x}GeTe_2$ were grown by the chemical vapor transfer method with iodine (I_2) as the transport agent. Starting materials comprised of elemental Fe powder (99.99%), Co powder (99.99%), Ge powder (99.999%) and Te powder (99.999%) with a nominal molar ratio 6(1-y):6y:1:5 (y ~ 45-50%) were fully ground and mixed together inside the glovebox. 50 mg of iodine was added to the mixture. The starting mixture was then evacuated, back filled with 1/3 Argon and sealed inside the quartz tube with an inner diameter of 8 mm, an outer diameter of 12 mm and length of 120 mm. The sealed quartz tube was placed horizontally inside a muffle furnace during the growth. The reaction temperature was set to 750 ºC under isothermal conditions for up to two weeks. Small and thin single crystals were harvested by quenching the furnace at 750 ºC in air. Excess iodine was removed from the surfaces of the crystals with ethanol.

Single-crystal XRD

XRD Measurements for the $(Fe_{0.5}Co_{0.5})_{4.87}GeTe_2$ single crystal were performed on a Rigaku XtaLAB P200 equipped with a MicroMax 007HF rotating anode and a Pilatus 200K hybrid pixel array detector. Room temperature data were collected using Mo Kα radiation (λ = 0.71073 Å). Data processing was done with CrysAlisPro and included a multi-scan absorption correction applied using the SCALE3 ABSPACK scaling algorithm within CrysAlisPro.[49] A solution was found using ShelXT[50] in space group $P6_3mc$ (No. 186). An inversion twin law was applied to the structural model. Four sites were split 50:50 between Fe and Co (sites 1, 3-5) and one site was split 44:44 between Fe and Co (site 2), based on the freely refined occupancy observed at each site. This is consistent with the elemental composition observed by energy-dispersive X-ray spectroscopy (EDS). One tellurium atomic site occupancy was also allowed to freely refine the structure, resulting in occupancy of ~94%. This was also consistent with that observed via EDS. The displacement parameters and atomic coordinates of the Fe and Co atoms were fixed to be equal using the EADP and EXYZ commands, respectively.

DFT Calculations

All density functional theory calculations were performed with the VASP code, using the Perdew-Burke-Ernzerhof (PBE) exchange-correlation functional[39] and the projector-augmented wavefunction (PAW) potentials. We use a pairwise van der Waals correction via the zero damping DFT-D3 method of Grimme[51] in all calculations. A plane-wave basis with an energy cutoff of 700 eV was used for all calculations; total energies were converged to 0.01 meV and a threshold of ±0.02 eV/Å was used for the Hellman-Feynman forces on the atoms. A Hubbard[40] U of 0.3 eV is used for Co and Fe d-orbitals. A k-grid of $11\times11\times7$ is used for 1x1x1 stoichiometric unit cells (ferromagnetic ABC phase) while a k-grid of $7\times7\times7$ is used for all other calculations for 1x1x2 unit cells. Methfessel-Paxton smearing was used for all Brillouin zone integrations with $\sigma = 0.04$ eV. All calculations were spin polarized, assuming collinear order. In all calculations, the Fe1/Co1 atoms were fixed to the 1a site. PAW potentials were used that treated as valence $5p^4 5s^2$ for Te, Ge ions used $4p^2 4s^2$ for Ge, $3d^7 3p^6 4s^1 3s^2$ for Fe, and $3d^8 3p^6 4s^1 3s^2$ for Co.

Electrical and magnetic measurements

High-quality FCGT nanoflakes were prepared on 100 nm SiO_2/Si substrates by means of mechanical exfoliation. E-beam lithography was utilized to pattern the samples, and then 3 nm Cr/150 nm Au was deposited with e-beam evaporation to fabricate Hall bar devices. The temperature-dependent resistance and Hall effect measurement were carried out in a CRYOGENIC measurement system (2 K, 14 T) with the magnetic field applied perpendicular to the nanoflake plane. A constant 10 µA *d.c.* current was applied for all the electric measurements. Second harmonic Hall resistance was measured by using a lock-in technique (SR-830, Stanford Research Systems); An AC current with a low frequency (23 Hz) was applied. We monitored the temperature by the sample resistance to eliminate the heating effect. Magnetic characterizations were carried out with a superconducting quantum interference device magnetometer (Quantum Design, 2 K, 7 T), with the magnetic field applied along the out-of-plane and in-plane direction of the crystal.

ST-FMR

The test structure for ST-FMR measurements is comprised of AlO_x (2.5 nm)/$Co_{0.9}Fe_{0.1}$(12.5 nm)/ FCGT (21 nm)//SiO_2(100 nm)/Si substrate that was patterned into rectangular bars by e-beam lithography. The ST-FMR measurements were carried out using a home-built system. The in-plane external magnetic field was oriented at $45°$ with respect to the current direction. During the measurements, a microwave current with fixed power and frequency was injected into the device and a DC voltage was collected while sweeping the external magnetic field. Multiple scans were accomplished at different frequencies to obtain effective magnetization and spin-orbit torque efficiency. The ST-FMR signal can be fitted by: $V_{mix} = V_{sym}F_{sym} + V_{asym}F_{asym}$, where V_{sym} and V_{asym} are the amplitudes of the symmetric and antisymmetric components which are proportional to the in-plane damping-like torque and out-of-plane torques, respectively. The symmetric Lorentzian component is F_{sym} and the antisymmetric Lorentzian component is F_{asym},

$$F_{sym}(H_{ext}) = \Delta H^2 / [(H_{ext} - H_r)^2 + \Delta H^2],$$

$$F_{asym}(H_{ext}) = \Delta H^2 (H_{ext} - H_r) / [(H_{ext} - H_r)^2 + \Delta H^2]$$

where ΔH is the linewidth of the V_{mix} curve, H_{ext} is the external magnetic field, and H_r is the resonance field. The effective magnetization (M_{eff}) of FCGT/$Co_{0.9}Fe_{0.1}$ bilayer is obtained by fitting the H_r verse resonance frequency (*f*) with the Kittel formula:

$$f = \left(\frac{\gamma}{2\pi}\right) ¿ ¿,$$

where, ɤ is the gyromagnetic ratio and H_k is the in-plane anisotropy field.

The charge-to-spin conversion coefficient (ξ) is the ratio of the spin current density to RF current density,

$$\xi = \left(\frac{V_{sym}}{V_{asym}}\right)\left(\frac{e \mu_0 M_s t}{\hbar}\right)[1 + (4\pi M_{eff}/H_{ext})]^{0.5}$$

where, M_s is the saturation magnetization and *t* is the thickness of the $Co_{0.9}Fe_{0.1}$.

Magnetic Force Microscopy (MFM)

MFM experiments were performed using scanning probe microscopy (MFP-3D, Asylum Research) at zero magnetic field. The MFM tip has a 40 nm cobalt alloy coating. The magnetic coating was magnetized perpendicular to the cantilever. The resonance frequency of the cantilever is ~ 75 kHz and the force constant is ~ 2.8 N/m. During the MFM imaging, the

distance between the tip and sample was maintained at a constant distance of 100 nm in a frequency-modulation mode. In order to prevent the surface oxidation of FCGT in air, a 5-nm Au capping layer was deposited over the FCGT flakes once the exfoliation was completed.

Lorentz (S)TEM

A polypropylene carbonate (PPC)/Polydimethylsiloxane (PDMS) stamp was used to transfer the FCGT nanoflakes from SiO_2/Si substrates onto commercial TEM grids. Samples were transferred using a 3-axis stage to pick up FCGT from SiO_2/Si with PPC after a heating process at 90 ℃ and a subsequent cooling to 60 ℃. Then, the FCGT was released onto TEM grids after the second heating to 90 ℃. Finally, the residual PPC was dissolved in acetone for a clean surface of FCGT. Four-dimensional (4D) Lorentz scanning transmission electron microscopy (LSTEM) experiments using an electron microscopy pixel array detector (EMPAD) was performed, where the 2D electron diffraction pattern was recorded over a 2D grid of real space probe positions, resulting in 4D datasets. Experimental data were acquired using an FEI Titan operated at 300 keV with ~0.34 mrad semi-convergence angle, having a probe of ~3.5 nm FWHM (full-width at half-maximum). The LSTEM mode was realized with a new plugin which allows the continuous tuning of magnetic fields from 0 mT (residual field <2 mT) by adjusting the current of the objective lens. The magnetic field near the sample position was calibrated by using a custom-made Hall chip mounted on an electrical biasing holder (*Protochips inc*.). The magnetic deflection angle was determined by using a combination of edge detection and cross-correlation method with sub-pixel precision.[47]

STEM

Cross-sectional TEM specimens were prepared on the same plan-view samples, using an FEI Strata 400 focused ion beam (FIB) with a final milling step of 2 keV to reduce damage. The initial sample surface was protected from ion-beam damage by depositing carbon and platinum layers prior to milling. The cross-sectional TEM specimen has a thickness of ~10 nm as determined by convergent beam electron diffraction analysis. HAADF-STEM images were recorded by using a Cs-corrected FEI Titan operated at 300 keV, with beam semi-convergence angle of 21.4 mrad and beam current of 20 pA.

STEM simulation

The STEM simulations were carried out using the µSTEM software[52], with neutral atomic scattering factors of Waasmaier & Kirfel[53]. The atomic coordinates were taken from single-crystal XRD refinements and density functional theory calculations for the AA' and AA stackings, respectively. The HAADF-STEM images of FCGT were simulated using a 300 keV electron probe with semi-convergence angle of 21.4 mrad, annular dark-field collection angles of 70-200 mrad, and sample thickness of 70 nm. Here the simulations were carried out with a maximum scattering angle of 10.5 $Å^{-1}$ (204.1 mrad), and a real space sampling of 4.35 probe positions per Angstrom. The thermal diffuse scattering effect was included with the frozen-phonon approximation, with 20 transmission functions and 150 Monte Carlo steps per probe position.

EELS measurements

Electron energy loss spectroscopy (EELS) mapping was performed using K3 Gatan direct electron detector installed at the back end of a Gatan continuum spectrometer in the TEAM I microscope at 300 kV. The probe angle, collection angle and current used for EELS acquisition were 20 mrad, 50 mrad and 100 pA respectively. The thickness of the samples determined from t/λ (t is the thickness and λ is a constant related to mean-free path in the elastic scattering of electron beam) ratio was around 10-20 nm for the AA and AA' configuration. The spectral EELS maps were generated by integrating the intensity of Fe, Co, Te and Ge after subtracting a power law background. The EELS maps and EELS line profiles were processed using Hyperspy.[54]

Magnetic induction field simulation for Lorentz (S)TEM

Magnetic induction field simulated from Bloch-type and Néel-type skyrmions were calculated from the magnetization distribution of an isolated skyrmion generated using the 360° domain wall model[33,55,56]. For simulation inputs, the diameter and domain wall widths of skyrmions are set to 90 nm and 4.2 nm, respectively. The saturation magnetization M_s is set to 301.6 kA/m, and sample thickness to 110 nm.

Micromagnetic simulation

Micromagnetic simulations were performed using the GPU-accelerated finite mesh package MuMax3.[57] To reproduce the experimentally observed spin textures, simulations were run over a range of DMI parameters close to the value estimated from experimental data. The parameter scans are presented as mosaics where each tile is a 1×1 μm^2 rendering of the z-component of magnetization from a single simulation.

Simulations incorporated the dipole-dipole interaction and finite temperature. Periodic boundary conditions were used since the simulated area 1×1 μm^2 is smaller than the actual sample. The parameters in the Hamiltonian are exchange constant A, 1st order uniaxial anisotropy K, saturation magnetization m_s, and interfacial Dzyaloshinskii Moriya interaction constant D. In these simulations $A = 4\times10^{-12}$ J/m, $K = 0.24\times10^6$ J/m^3, $M_s = 301$ kA/m, T = 293 K, and D is varied over the range of 0.75 mJ/m^2 to 1.3 mJ/m^2. The cell size of $3.9 \times 3.9 \times 3.1$ nm^3 is below the

exchange length $l_{ex} = \sqrt{\dfrac{2A}{u_o M_s^2}}$ 9.8 nm. The simulation area is 1 μm $\times$ 1 μm $\times$ 110nm. A cell size of $3.9 \times 3.9 \times 3.1$ nm^3 is used. The simulation was initialized in a random state. The initial state is then relaxed using the MuMax3 standard relax function and advanced using a time evolver for 100 ns to incorporate thermal effects. Two sets of simulations were performed. The first set was performed without an applied magnetic field and relaxes to a domain state. The second set was performed with an applied field of 139 mT along the z-axis and relaxes to a Skyrmion lattice state.
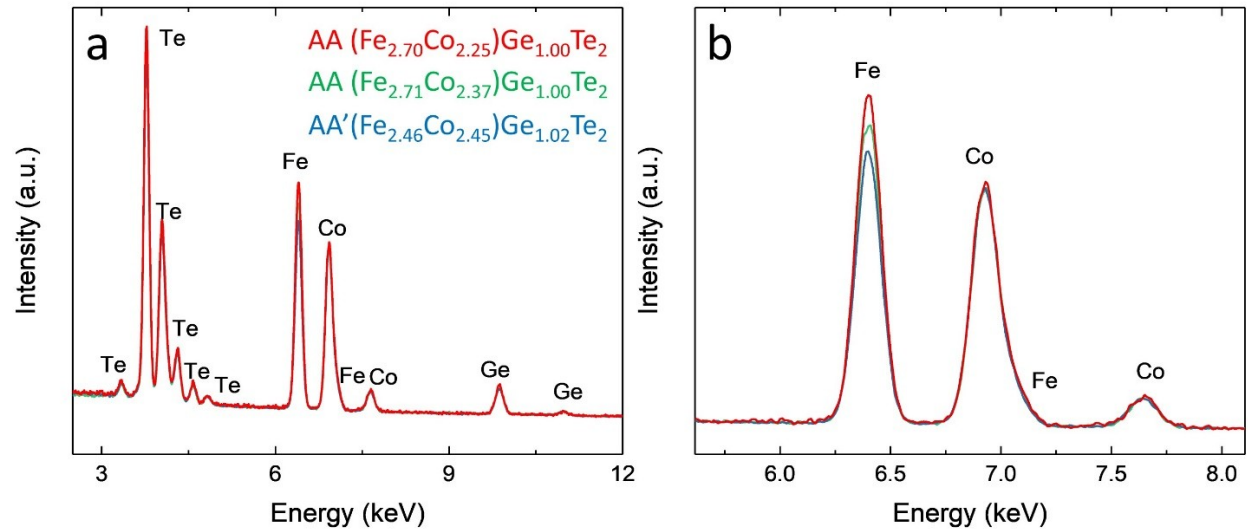
Fig. S1 Energy Dispersive X-ray Spectroscopy (EDS) of FCGT single crystal. a, The EDS spectrum of AA (45% and 47%) and AA' (50%) phase FCGT single crystals. **b,** The zoomed-in spectrum near the Fe and Co peaks.
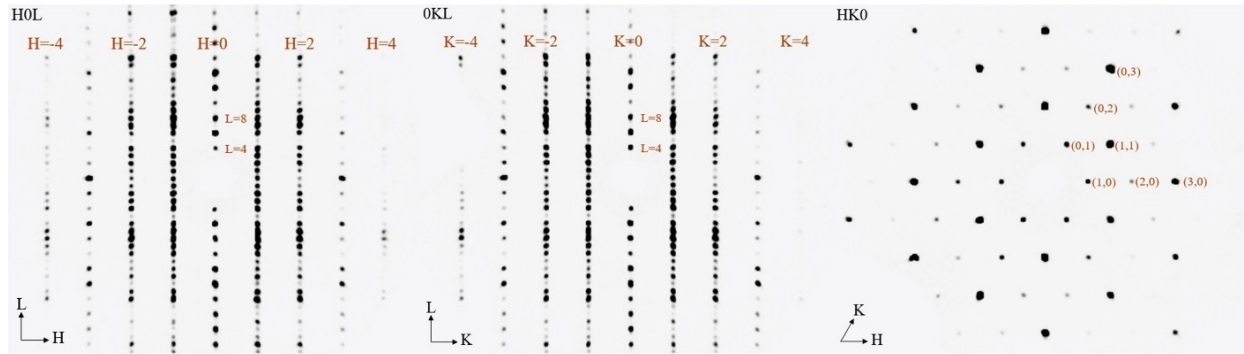
Fig. S2 Single crystal X-ray diffraction of AA' stacked FCGT. X-ray diffraction data of FCGT single crystals indexed in the H0L, 0KL and HK0 planes. The FCGT crystals display a wurtzite structure with a space group P6$_3$*mc* from the refinement of scattering data. Wurtzite FCGT is a hexagonal polar magnet metal which belongs to the C_{6v} point group satisfying the prerequisite for hosting the Néel-type skyrmion and Rashba spin-orbit coupling.
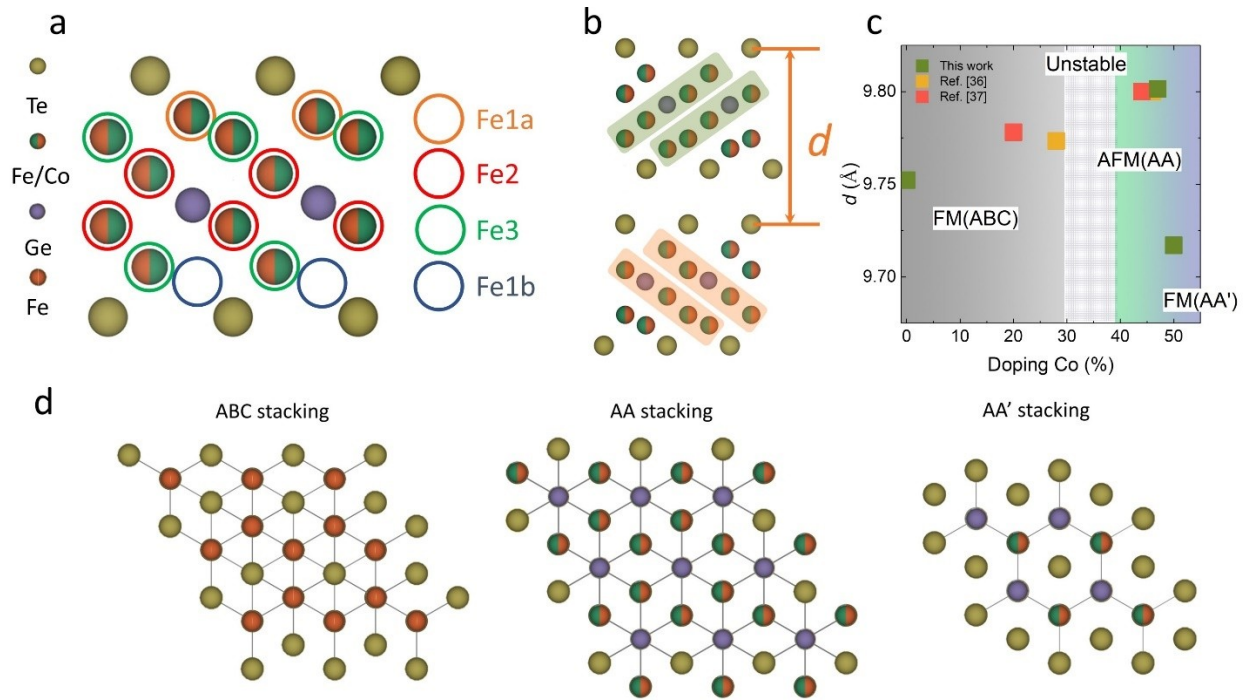
Fig. S3 Sublayer lattice constant along c axis with different cobalt concentrations. a, Schematic of FCGT sublayer with atomic types. Fe/Co sites are labeled as Fe1a(orange), Fe2 (red), Fe3 (green) and Fe1b (blue). **b,** Side profile atomic rendering of FCGT for AA' stacking viewed along the [110] zone axis. **c,** As the cobalt concentration increases, the sublayer lattice constant correspondingly increases. At a cobalt concentration of 50%, the sublayer lattice constant drops abruptly due to the competition between vdW and Coulombic interaction. In the high cobalt doping region, the AA' phase can be stabilized. **d,** The top view of the crystal structures for ABC stacking, AA stacking and AA' stacking
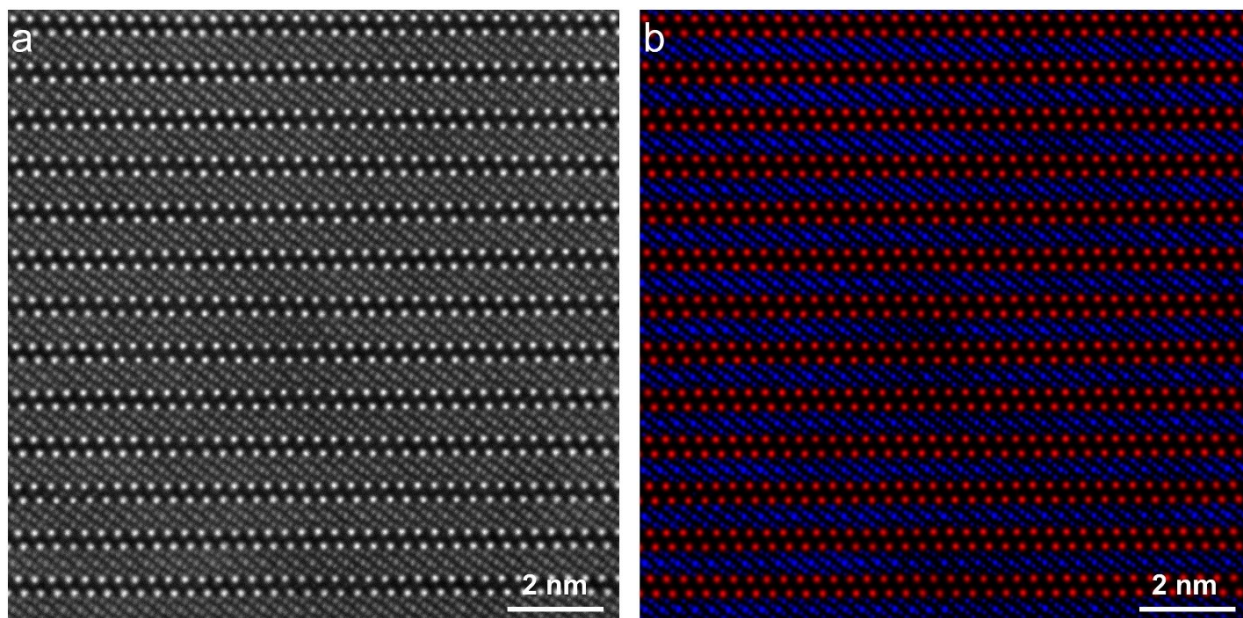
Fig. S4 Experimental HAADF-STEM image of AA FCGT (y=0.45) showing sublattices of Te and zag-FCG. a, Raw experimental image. **b**, False colored sublattices of Te in red and zag-FCG in blue aided by 2D Gaussian fitting of atomic column positions.
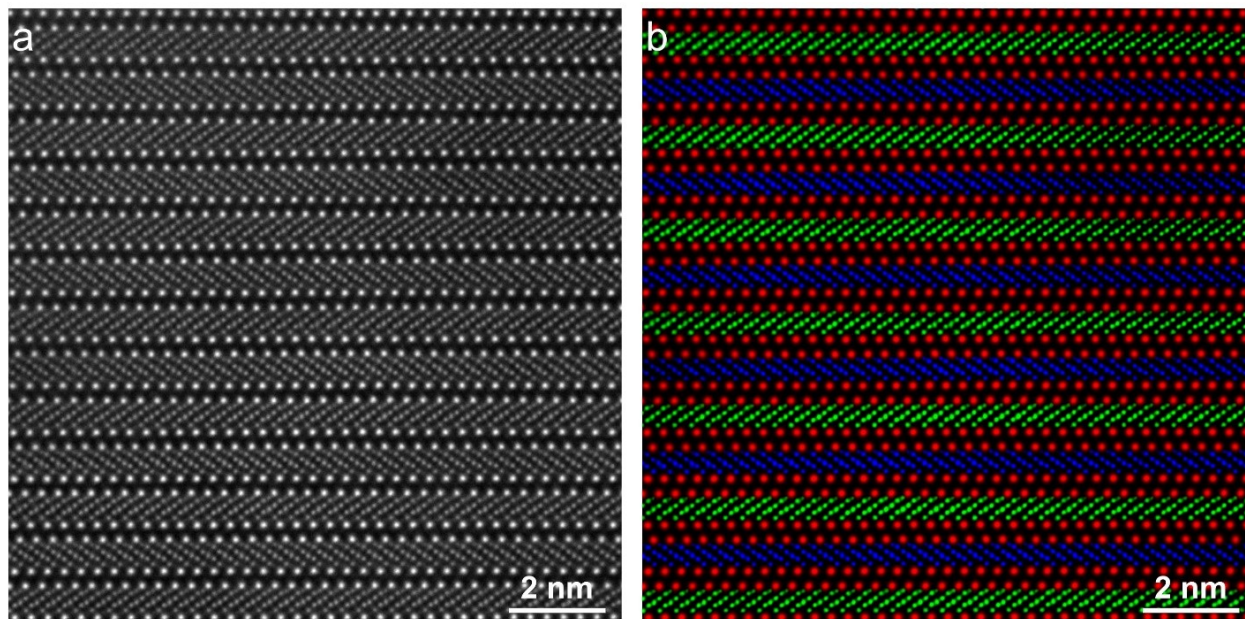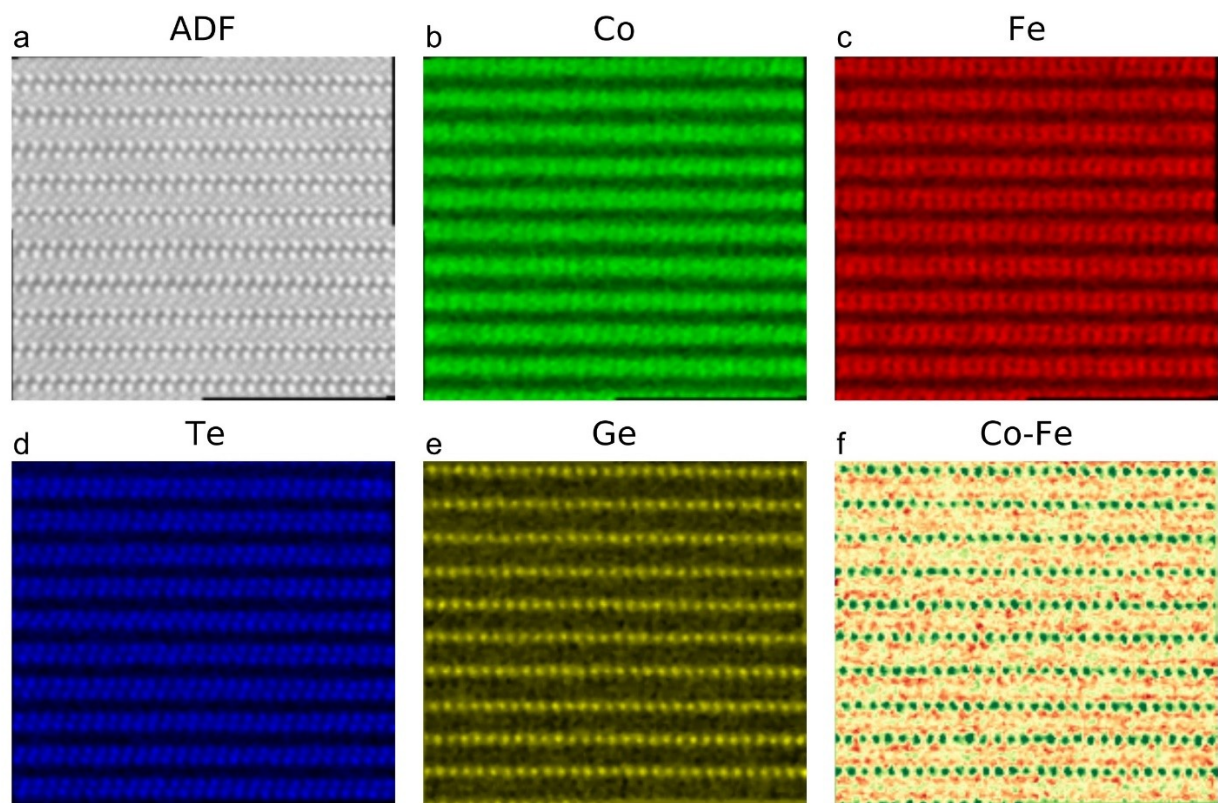
Fig. S5 Experimental HAADF-STEM image of AA' FCGT (y=0.50) showing sublattices of Te, zig-FCG, and zag-FCG. a, Raw experimental image. **b**, False colored sublattices of Te in red, zig-FCG in green, and zag-FCG in blue aided by 2D Gaussian fitting of atomic column positions.

Fig. S6 EELS mapping of AA phase FCGT. a, Simultaneous HAADF, elemental EELS maps

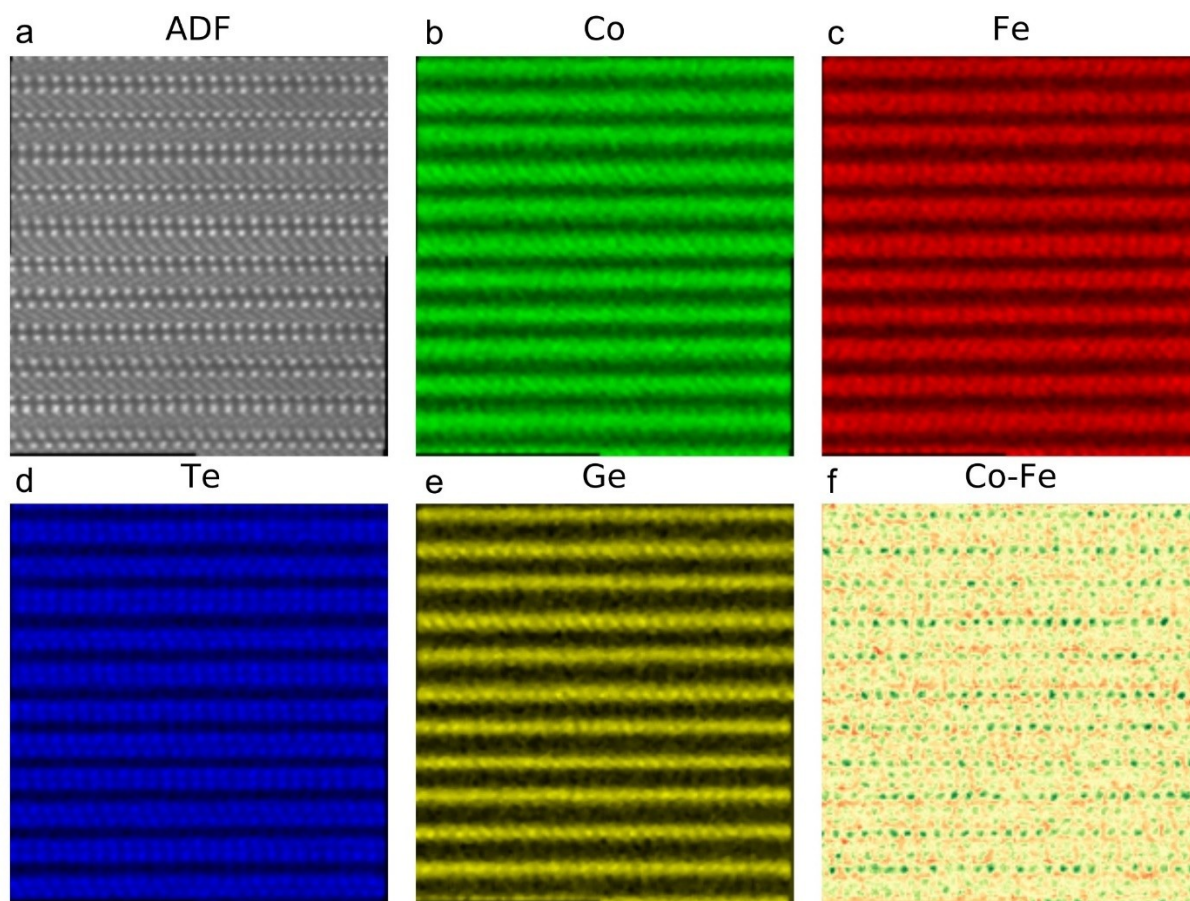for **b** Co, **c**, Fe, **d**, Te and **e**, Ge. f, Normalized intensity difference maps (Co-Fe) for AA phase.

Fig. S7 EELS mapping of AA' phase FCGT. a, Simultaneous HAADF, elemental EELS maps for **b**, Co, **c**, Fe, **d**, Te, and **e**, Ge. f, Normalized intensity difference maps (Co-Fe) for AA' phase.
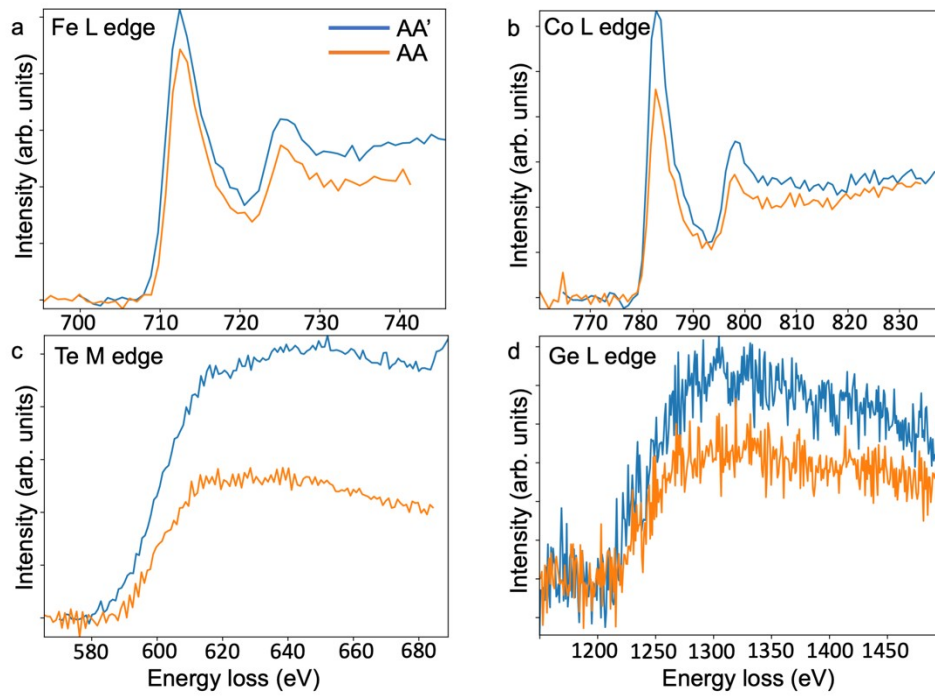
Fig. S8 EELS spectral signals of AA and AA' phase FCGT. a,b,c,d, Average EELS spectral

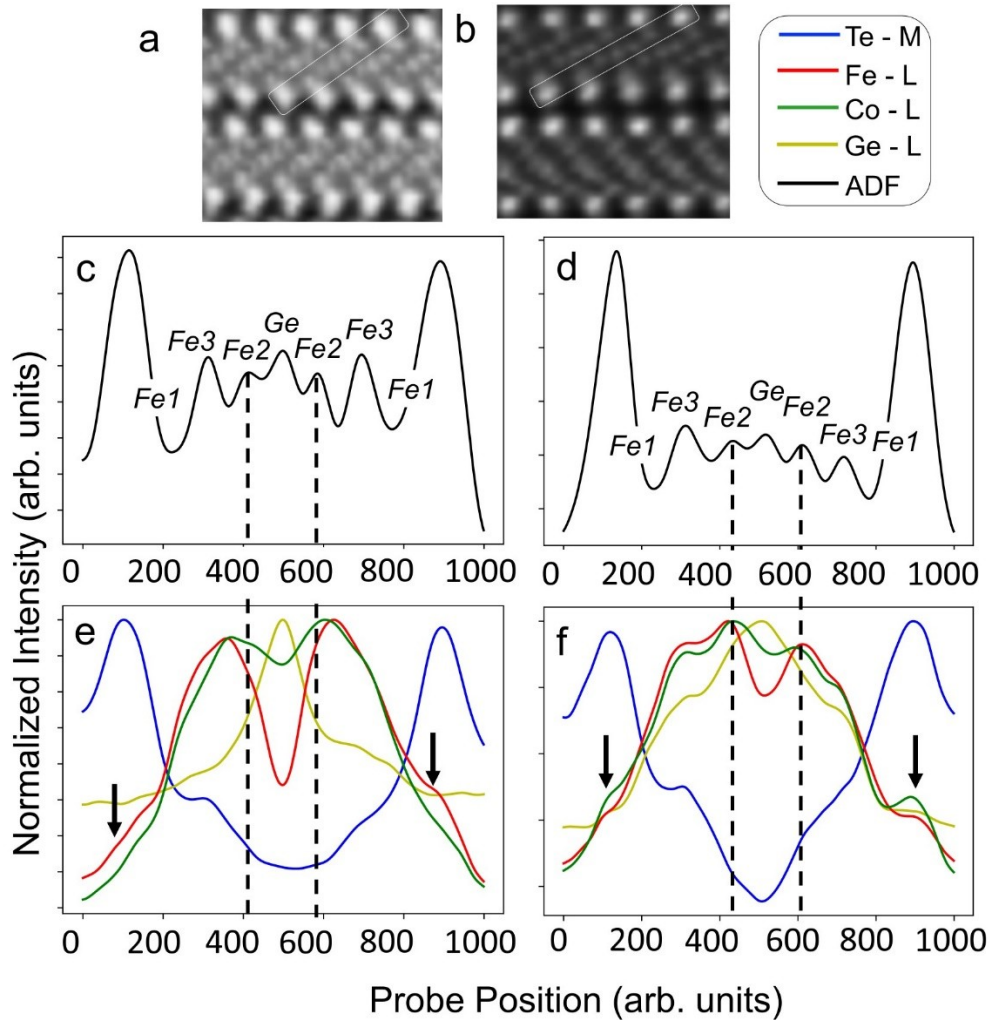signals from Fe L edge, Co L edge, Te M edge and Ge L edge for AA and AA' phase.

Fig. S9 EELS Line profile. Magnified annular dark-field (ADF) images of (**a**) AA phase and (**b**) AA' phase. (**c**) sum of ~50 EELS line profiles for Te-M, Fe-L, Co-L and Ge-L edge extracted along the atomic plane shown in ADF (**a, b**) for (**c**) AA and (**d**) AA' phase, respectively. Simultaneous summed line profile of ADF for (**e**) AA and (**f**) AA' phase. The legend for the line profile is presented beside (**b**). It is evident that there is Co enrichment in Fe2 sites in AA phase and AA' phase. However, at Fe1 site (indicated by the arrow), there is Fe enrichment in the AA phase and Co enrichment in the AA' phase.

Structure	E_{GS} (meV/f.u.)	*a*	*c*	Intralayer
Fe_5GeTe_2 **ABC (FM)**	0	0%	0%	0%
Fe_5GeTe_2 **AA (AFM)**	-4	0.0%	+0.1%	+0.4%
Fe_5GeTe_2 **AA' (FM)**	-12	+0.1%	-1.7%	-0.3%
Co_5GeTe_2 **ABC (FM)**	0	0%	0%	0%
Co_5GeTe_2 **AA (AFM)**	-8	+0.2%	+0.3%	+0.7%
Co_5GeTe_2 **AA' (FM)**	0	-0.2%	-1.3%	+0.4%

Table S1 DFT-computed relative ground-state energies & crystallographic lattice parameters for $(Fe_yCo_{1-y})_5GeTe_2$ compounds. Columns include the electronic ground-state energy (meV/f.u.), the in-plane and out-of-plane lattice parameters *a* and *c*, and the intralayer spacing within a van der Waals layer bounded on either side by Te planes. All computed values are presented with respect to either the Fe_5GeTe_2 or Co_5GeTe_2 chemical endpoint compounds with ABC-phase and ferromagnetic order. The optimized DFT-PBE+U+D3 Fe_5GeTe_2 ABC (FM) structure has a = 3.975 Å and c = 9.716 Å with interlayer spacing d = 6.641 Å. The optimized DFT-PBE+U+D3 Co_5GeTe_2 ABC (FM) structure has a = 3.975 Å and c = 9.527 Å with interlayer spacing d = 6.539 Å. Results with specific magnetic orders for each structural phase have been selected based on experimentally observed ordering.
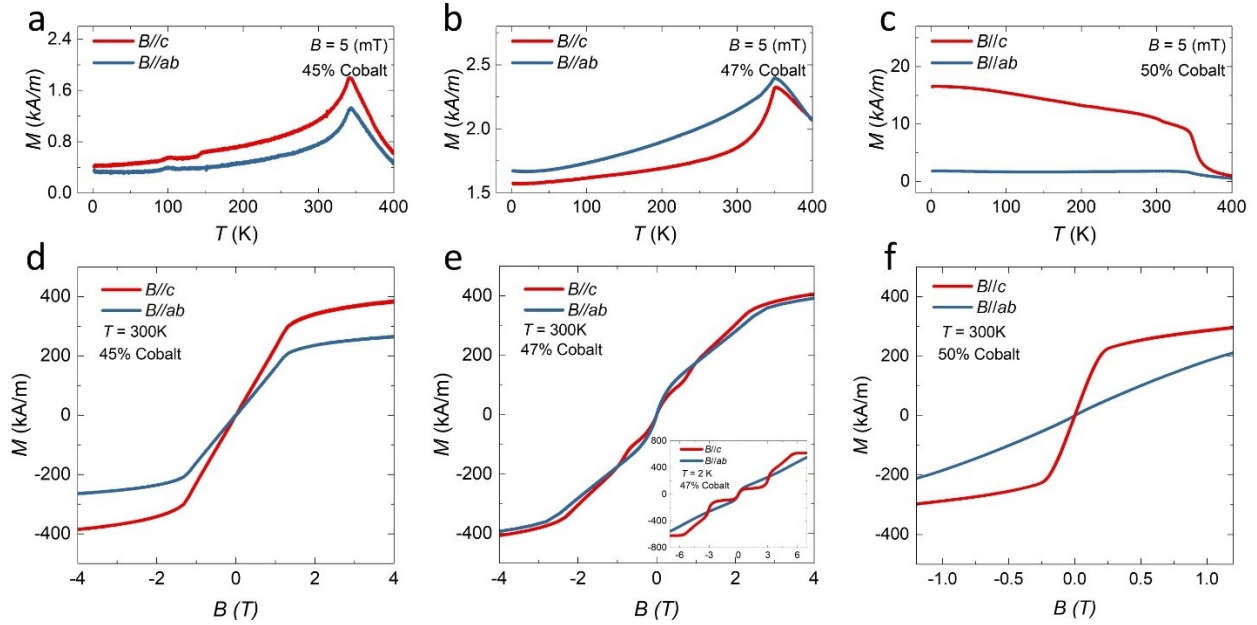
Fig. S10 Doping-concentration-dependent magnetic properties of FCGT single crystals. Temperature-dependent magnetization of FCGT single crystals was obtained with a magnetic field of 5 mT. **a,b,** The magnetization of FCGT (45% and 47%) increases with increasing temperature and reaches a maximum at ~ 343K and 350 K, respectively, exhibiting an antiferromagnetic (AFM) to paramagnetic phase transition. **c,** The magnetization of FCGT (50%) decreases with increasing temperature and vanishes at ~350 K, showing a ferromagnetic (FM) to paramagnetic phase transition. Fig. **d**, **e**, **f** show isothermal magnetization curves of FCGT (45%, 47% and 50%) single crystals at room temperature. **d,** For a 45% cobalt concentration, a spin-flop transition is observed near 1.5 T. **e,** The magnetic field dependence of magnetization for a 47% cobalt concentration shows a step-like shape indicating a mixture of AFM and FM phases. Inset of **e** shows the isothermal M-H curves at 2K **f,** The isothermal M-H curves of the FCGT (50%) crystal exhibit an easy axis along the c-direction. A saturation magnetization, $M_S = 301.6$ kA/m and an effective anisotropy, $K_{u,eff} = 2.4 \times 10^5$ J/m^3 are estimated.
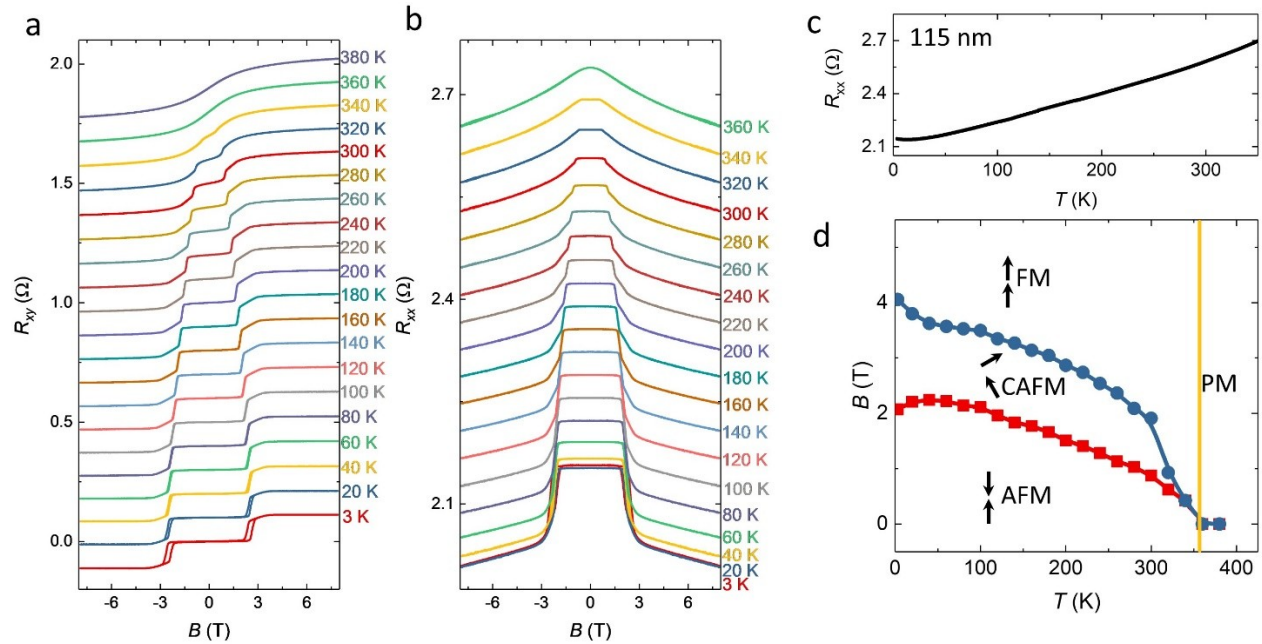
Fig. S11 Magnetotransport measurements of an AA phase FCGT nanoflakes. a, **b**, Anomalous Hall resistance and magnetoresistance at various temperatures for the 115-nm-thick AA phase FCGT nanoflake. The results clearly show that a spin flop transition occurs at a relatively high magnetic field of ~2.5T at 3K and ~1T at 300K. Above this field, it transitions to a ferromagnetic single domain. **c,** Temperature dependence of the longitudinal resistance exhibits a metallic behavior. **d**, H-T phase diagram showing antiferromagnetic (AFM) phase, canted-antiferromagnetic (CAFM) phase and paramagnetic (PM) phase.
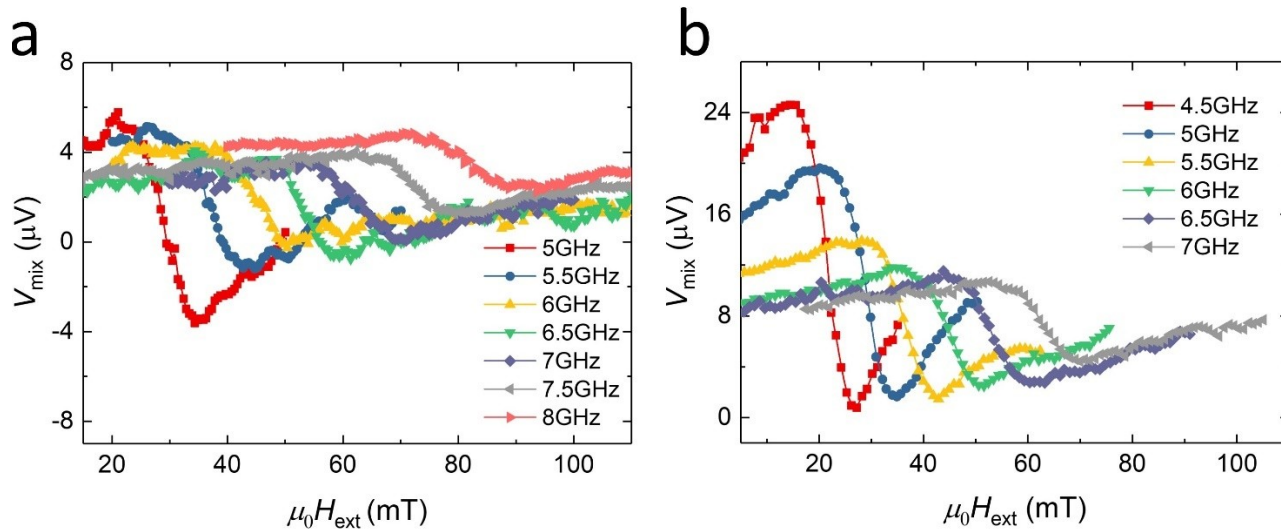
Fig. S12 Frequency dependence of V_{mix} for FCGT/Co$_{0.9}$Fe$_{0.1}$ bilayer. a, b, Frequency dependence of V_{mix} versus magnetic field for FCGT/Co$_{0.9}$Fe$_{0.1}$ bilayer obtained at 15 dBm and 18dBm.
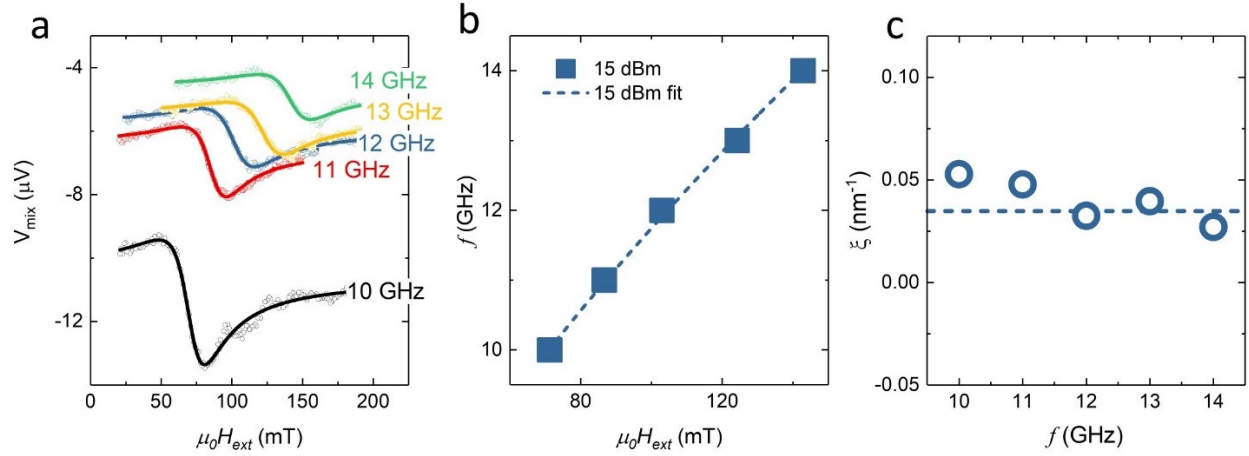
Fig. S13 ST-FMR measurements of an AA phase FCGT nanoflakes. a, The ST-FMR signal of an AA phase FCGT(73 nm) /$Co_{0.9}Fe_{0.1}$ (12.5 nm) sample at 15 dBm and varying frequency, with an external magnetic filed oriented 45° to the current direction. **b,** ST-FMR frequency as a function of resonance field; the blue line is a fit to the Kittel formula. **c,** Charge to spin conversion coefficient (ξ) as a function of frequency at 15 dBm, ~ 0.034 nm^{-1}.

Second-harmonic Hall measurements

The second-harmonic Hall voltage measurement in a 100-nm thick FCGT single layer was performed. A magnetic field parallel to the ac current ($I = I_0 \sin(\omega t)$, where $I_0 = 6$ mA and frequency $\omega = 23$ Hz) direction was applied,. As the following Fig. S14 shows, the second harmonic Hall resistance is anti-symmetric with in-plane magnetic field. A kink clearly occurs around the magnetic anisotropy field $H_K = 1.3$ T which is determined by magnetic hysteresis loop measurements. When H_x is larger than H_K (the anisotropy field), the second harmonic Hall resistance is generated by the magnetization oscillation from the ac current, and the R_{xy}^{2w} can be written as:

$$R_{xy}^{2w} = \frac{-1}{2} \frac{R_{AHE} H_{eff}}{|H_x| - H_K} + R_{Offset}^{2w}, \tag{1}$$

where R_{AHE} is the out-of-plane anomalous Hall resistance. By fitting the result of Fig.S14 using equation (1), the effective field H_{eff} generated by the spin-orbit torques can be calculated to be 1.25 Oe. From this, the charge-to-spin current conversion efficiency can be written as:

$$\xi = \frac{2 e M_s H_{eff}}{\hbar J_x}, \tag{2}$$

where $M_s = 301.6$ KA/m, $J_x = 4.7 \times 10^5$ A/cm^{-2} Therefore, we calculate the charge to spin conversion efficiency, $\xi = 0.024$ nm^{-1}.
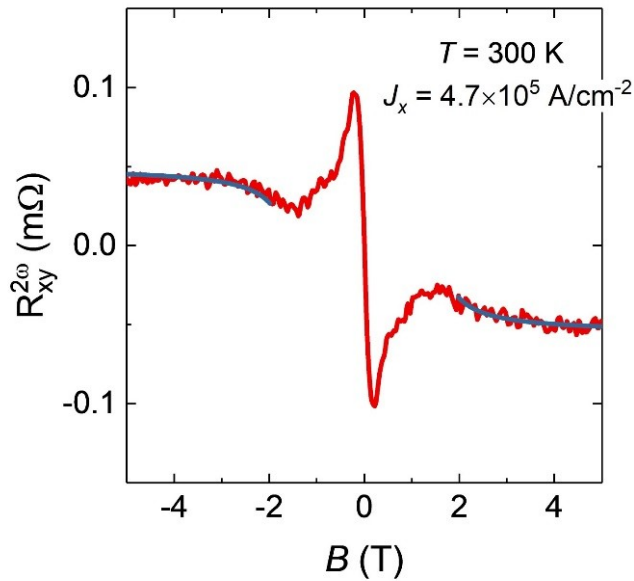
Fig. S14 Second harmonic Hall resistance. In-plane magnetic field dependence of second harmonic Hall resistivity R_{xy}^{2w} for the 100-nm thick FCGT sample. Blue line indicates the fitting to equation (1).
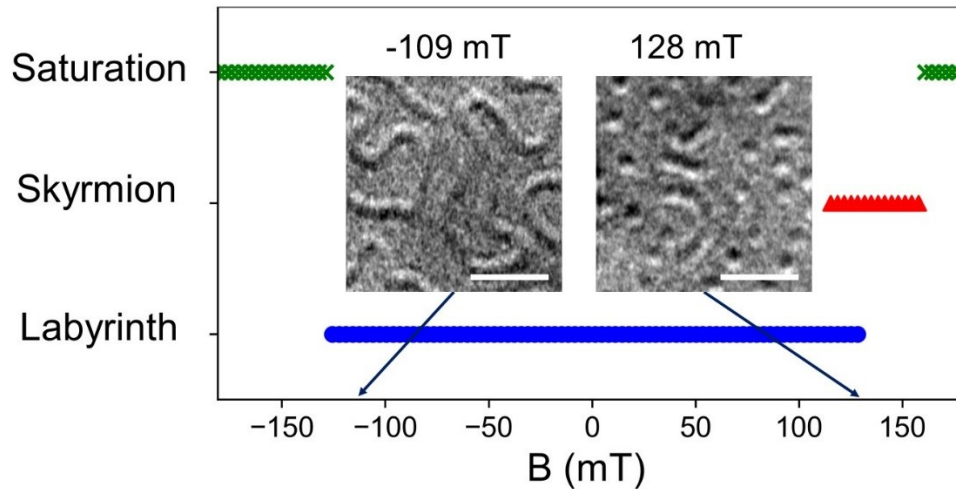

Fig. S15 The evolution of spin texture with varying magnetic fields. The phase diagram of magnetic texture versus applied magnetic field for a 110-nm-thick FCGT flake, with the external field swept from -180 mT to 180 mT at room temperature. Inset, two representative LTEM images acquired at -109 mT and 128 mT showing the serpentine domains and their mixture with skyrmions, respectively. It is clearly shown that the external magnetic field serves as an effective parameter to engineer the domain structures between a skyrmion (red triangle), saturated single domain (green cross), and labyrinthine (blue circle) phases. Scale bars in the insets are 500 nm. Lorentz TEM images were acquired at a defocus of +4 mm.
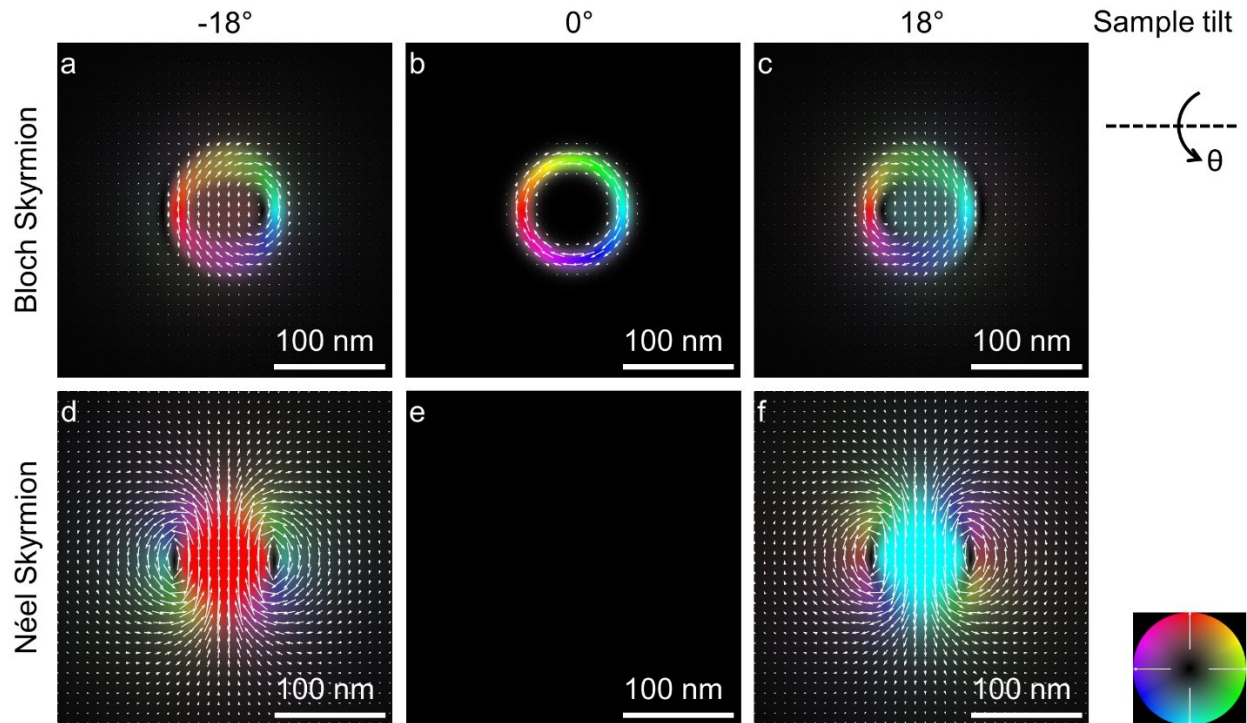
Fig. S16 Simulated magnetic induction field from Bloch-type and Néel-type Skyrmions at different sample tilt angles. Magnetic induction field distribution for a (**a-c**) Bloch skyrmion and a (**d-f**) Néel skyrmion at tilt angles of -18°, 0°, and -18° were calculated from the magnetization distribution of an isolated skyrmion generated using the 360° domain wall model. Since the phase gradient obtained from L-STEM is proportional to the induction field, the "bi-skyrmion" shape is a signature of a Néel-type skyrmion observed at a tilted angle. The simulation was carried out using a skyrmion diameter of 90 nm, and a domain wall width of 4.2 nm, a saturation magnetization M_S of 301.6 kA/m, and a sample thickness of 110 nm. The slight shape difference between simulations and experiments may be explained by the distorted skyrmion shape (elongation) resulting from the experimentally applied external magnetic field.
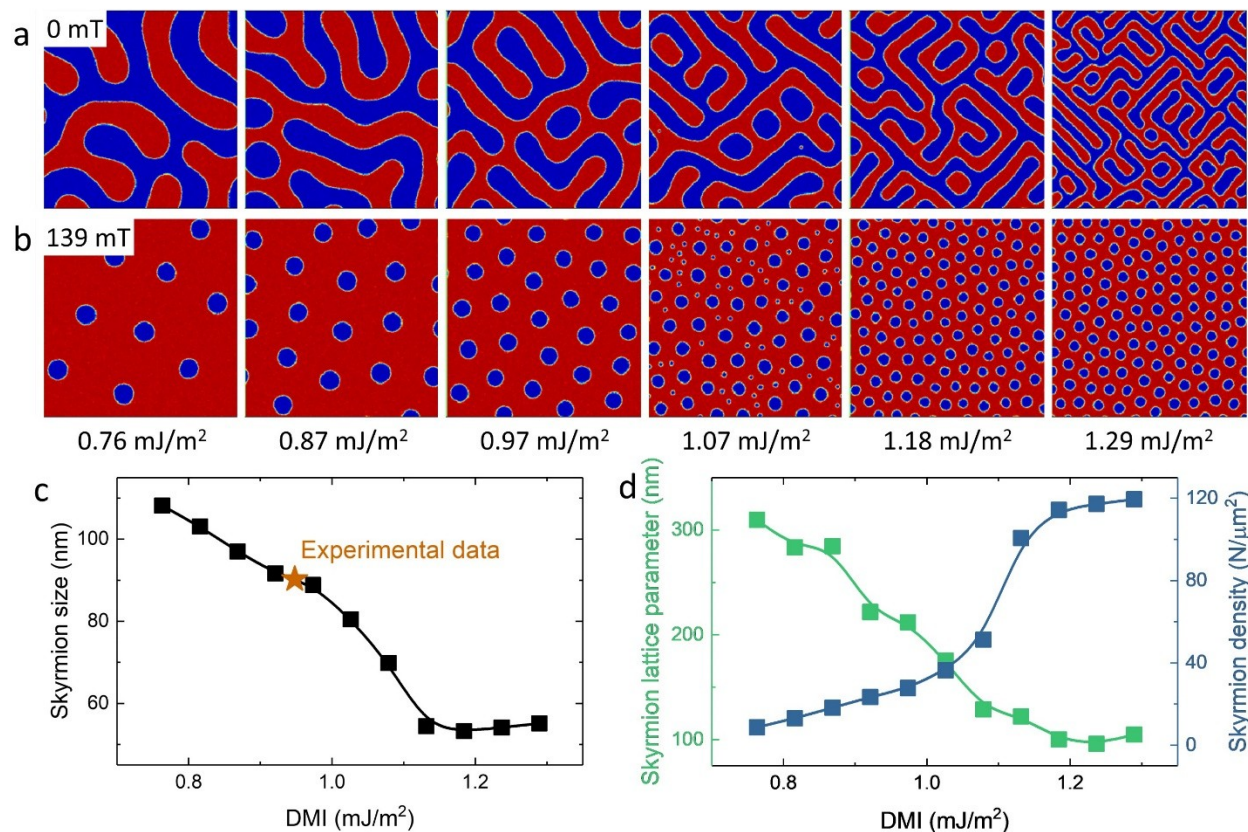
Fig. S17 Micromagnetic simulation. DMI constant (0.75~1.3 mJ/m^2) dependent domain pattern at applied an external magnetic field of 0 mT (**a**) and 139 mT (**b**). The image size is 1μm×1μm. **c**, DMI constant dependence of skyrmion size at the 139 mT exhibits that the skyrmion size decrease as the DMI constant increasing. d, DMI constant dependence of skyrmion lattice parameter at 139 mT shows that the lattice parameter decreases and skyrmion density increase with the DMI constant increasing. The LTEM results can be reproduced by the micromagnetic simulation which gave a DMI constant value of ~0.95 mJ/m^2.
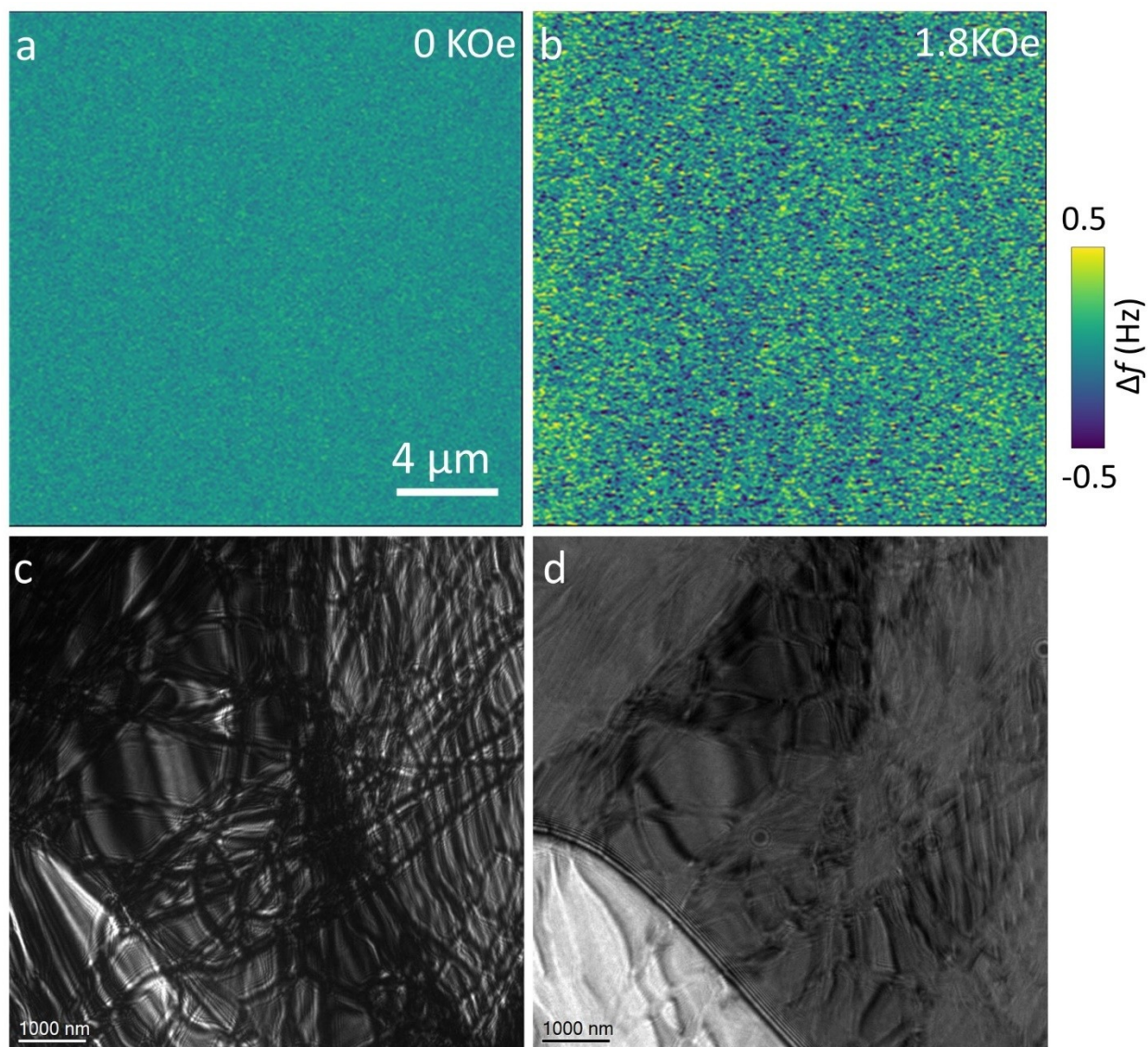
Fig. S18 Spin texture measurements for AA phase FCGT bulk. MFM images of an AA phase bulk crystal FCGT at 0 Oe (**a**) and 1.8 kOe (**b**) and room temperature. These images show no contrast. The scale bar is 4 μm. Lorentz TEM images of a 242 nm-thick AA phase FCGT. No obvious magnetic contrast was observed at various tilting angles of (**c**) 0º and (**d**) 25º. LTEM images were taken with a +4 mm defocus and under magnetic field of < 2 mT.

Reference:

48   Rigaku Oxford Diffraction v. 1.171.40.84a (Rigaku Corporation, Oxford, UK, 2015).
49   Sheldrick, G. SHELXT - Integrated space-group and crystal-structure determination. *Acta Cryst.* **A71**, 3-8, (2015).

50   Grimme, S., Antony, J., Ehrlich, S. & Krieg, H. A consistent and accurate ab initio parametrization of density functional dispersion correction (DFT-D) for the 94 elements H-Pu. *J. Chem. Phys.* **132**, 154104, (2010).

51   Allen, L. J., AJ, D. A. & Findlay, S. D. Modelling the inelastic scattering of fast electrons. *Ultramicroscopy* **151**, 11-22, (2015).

52   Waasmaier, D. & Kirfel, A. New analytical scattering-factor functions for free atoms and ions. *Acta Crystallogr.* **Sect. A 51** 416–431, (1995).

53   Francisco de la Peña, E. P., Vidar Tonaas Fauske, Pierre Burdet, Tom Furnival, Petras Jokubauskas,   Gaël Donval. . in *hyperspy/hyperspy: Release v1.6.2 (Version v1.6.2).* (http://doi.org/10.5281/zenodo.4683076, 2021).

54   Mansuripur, M. Computation of electron diffraction patterns in Lorentz electron microscopy of thin magnetic films. *J. Appl. Phys.* **69**, 2455-2464, (1991).

55   Romming, N., Kubetzka, A., Hanneken, C., von Bergmann, K. & Wiesendanger, R. Field-Dependent Size and Shape of Single Magnetic Skyrmions. *Phys. Rev. Lett.* **114**, 177203, (2015).

56   Vansteenkiste, A. *et al.* The design and verification of MuMax3. *AIP Adv.* **4**, 107133, (2014).